isvr Institute of Sound and Vibration Research

Active Vibration Control of a Beam using Piezoelectric Actuators

G. Gatti, M.J. Brennan and P. Gardonio

ISVR Technical Memorandum No 954

July 2005

University of Southampton

SCIENTIFIC PUBLICATIONS BY THE ISVR

Technical Reports are published to promote timely dissemination of research results by ISVR personnel. This medium permits more detailed presentation than is usually acceptable for scientific journals. Responsibility for both the content and any opinions expressed rests entirely with the author(s).

Technical Memoranda are produced to enable the early or preliminary release of information by ISVR personnel where such release is deemed to the appropriate. Information contained in these memoranda may be incomplete, or form part of a continuing programme; this should be borne in mind when using or quoting from these documents.

Contract Reports are produced to record the results of scientific work carried out for sponsors, under contract. The ISVR treats these reports as confidential to sponsors and does not make them available for general circulation. Individual sponsors may, however, authorize subsequent release of the material.

UNIVERSITY OF SOUTHAMPTON

INSTITUTE OF SOUND AND VIBRATION RESEARCH

DYNAMICS GROUP

Active Vibration Control of a Beam using Piezoelectric Actuators

by

G. Gatti, M.J. Brennan and P. Gardonio

ISVR Technical Memorandum No: 954

July 2005

Authorised for issue by
Professor M.J. Brennan
Group Chairman

Abstract

Piezoelectric materials have the ability to produce a contraction or extension when an electrical charge is applied to them. By integrating piezoelectric elements into slender structures, structural vibration and oscillations can be reduced by measuring them and controlling the actuators in real time. Such a composite structure is referred to as smart-structure. In this report the way in which piezoceramic actuators couple into, and excite a beam are briefly reviewed. Two different control strategies to control the global vibration of the beam, namely feedforward control and direct velocity feedback control, are then discussed and compared. Advantages and disadvantages of both the approaches are highlighted. Theoretical and off-line simulations using experimental data are presented and compared with experimental results.

Table of Contents

Table of Figures

Nomenclature

V : Applied voltage to piezoelectric actuator

E : Applied Electric field to piezoelectric actuator

d_{31} : Piezoelectric strain constant, i.e. strain along direction 1, for unitary electric field applied in direction 3.

x : Longitudinal, axial, direction along the beam

z : Transverse, out-of-plane, direction with respect to the beam

$\varepsilon(z)$: Strain distribution along the beam section

ε_1 : Strain along direction 1

ε_1^f : Unconstrained strain along direction 1

M_i : Induced moment by piezoelectric actuator

F_i : Induced force by piezoelectric actuator

t_p : Piezoelectric actuator thickness

Y_p : Young's modulus of the piezoelectric actuator

I_p : Moment of inertia of the piezoelectric actuator

d : Length of the piezoelectric actuator

t_b : Beam thickness

Y_b : Young's modulus of the beam

I_b : Moment of inertia of the beam

A_b : Beam section area

ρ_b : Beam mass density

M_b : Beam mass

Y : Young's modulus ratio

T : Thickness ratio

R : Strain ratio

q_n : n^{th} Modal amplitude

ϕ_n : n^{th} Mode shape

M_n : n^{th} Modal mass

ω_n : n^{th} Natural frequency

η : Structural damping

$w(x,t)$: Out-of-plane beam displacement (time domain)

$w(x)$: abbrev. for $w(x,t)$

$W(x,\omega)$: Out-of-plane beam displacement (freq. domain)

$W(x)$: abbrev. for $W(x, \omega)$

W_e : abbr. for $W(x_e)$

$V(x, \omega)$: Out-of-plane beam velocity (freq. domain)

$V(x)$: abbrev. for $V(x, \omega)$

V_e : abbr. for $V(x_e)$

$A(x, \omega)$: Out-of-plane beam acceleration (freq. domain)

$A(x)$: abbrev. for $A(x, \omega)$

A_e : abbr. for $A(x_e)$

M_P : Primary moment

M_S : Secondary moment

x_p : Position of the primary piezoelectric actuator along the beam

x_S : Position of the secondary piezoelectric actuator along the beam

$R(x_w, x_P)$: Receptance at position x_w due to moment pair excitation at position x_P

R_{wP} : abbrev. for $R(x_w, x_P)$

$Y(x_w, x_P)$: Mobility at position x_w due to moment pair excitation at position x_P

Y_{wP} : abbrev. for $Y(x_w, x_P)$

$T(x_w, x_P)$: Accelerance at position x_w due to moment pair excitation at position x_P

T_{wP} : abbrev. for $T(x_w, x_P)$

VKE : Vibrational kinetic energy

m_e : Mass of the e^{th} element

$G(\omega)$: Feedforward controller transfer function

J : Cost-function to be optimized, i.e. Kinetic energy reduction factor

g : Feedback gain

g_a : Signal conditioning gain

H_a : Accelerometer transfer funcion

H_i : Integrator transfer funcion

c_p : Piezoelectric actuator transfer function

1 – Introduction

The control of mechanical and structural vibrations is important in many fields. In manufacturing, where mechanical vibration degrades both the production rate and the quality of the end products; in civil engineering, where structural vibrations affect human comfort; in automotive and aerospace fields, where vibrations reduce component life and generate annoying noise.

Different approaches have been applied to suppress or reduce unwanted vibrations in the engineering field. Traditionally, passive dampers and isolators are used to attenuate mechanical vibrations [1, 2, 3], leading to so-called passive vibration control. Recent advances in digital signal processing and sensors and actuators technology have prompted interest in active vibration control [4, 5].

A typical active vibration control system is an integration of mechanical and electronic components with computer control. The main components of an active vibration control system are the mechanical structure influenced by the disturbance (creating unwanted vibrations), the sensors (to perceive the vibration), the controller (to intelligently make use of the signal from the sensor and to generate the appropriate control signal), and the actuator (to counteract the effect of the disturbance on the structure). Destructive interference, from the influence of the actuator, suppress or attenuate the unwanted disturbance on the structure. Various methods of active vibration control have been developed and they may be classified under two general categories: feedback and feedforward active vibration control. Among these two main categories, variations exist, each with advantages, disadvantages and limitations.

In this report, a feedforward control system and a feedback control system, with a velocity sensor/moment pair actuator, are studied and applied to a beam. The performances of the control systems are presented in terms of the global vibrational kinetic energy of the beam. For the feedforward approach, the optimal controller is derived. For the feedback approach, the optimum feedback gain is derived in a given bandwidth.

This report intends to emphasize the main differences between the two control strategies. Theoretical simulations, simulations based on experimental measurements (off-line experiments) and experimental results are then presented and discussed.

2 – Piezoelectric Elements and Coupling Models

Piezoelectric materials have the ability to produce an electrical charge when extended or contracted. They also produce an extension or contraction when an electrical charge is applied to them. Piezoelectric elements are relatively inexpensive, lightweight, easily shaped and bonded to or embedded into a variety of materials. They are produced as thin structures making it relatively easy to tailor them for more convenient use. Furthermore, depending on their shape, distributed piezoelectric elements may be used to detect motion at particular points in a structure (sensors) and exert forces and moments (actuators). The design and placement of these piezoelectric elements is obviously of great importance to achieve optimal performances. In this section, the main concepts and results from [6] are summarised here for completeness.

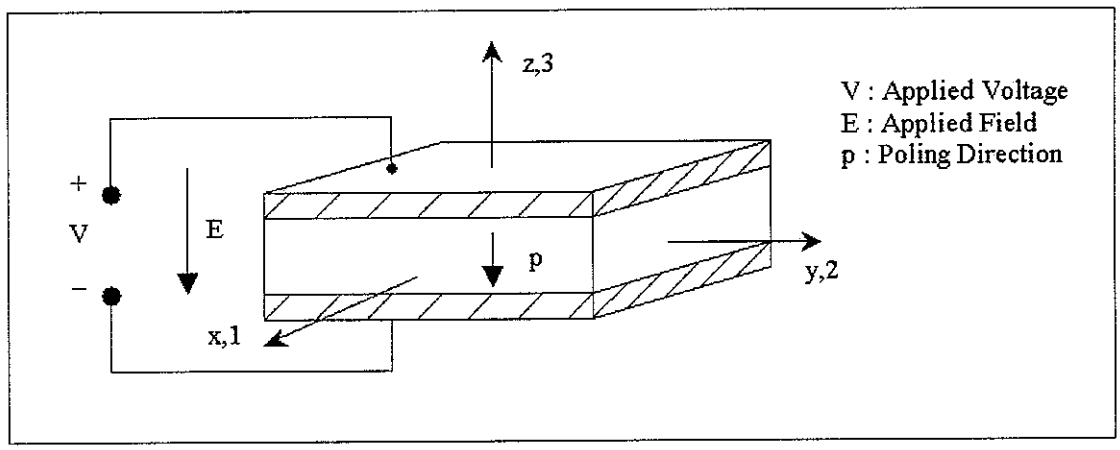

Figure 1 – Convention for directions in a piezoelectric element

In the one-dimensional case, a free piezoelectric element (assumed to be polarized along the z direction), as illustrated in Figure 1, is assumed to develop compressive or tensional strain in the x direction when activated by applying a voltage (V) in the z direction. The induced strain is determined by the sign and amplitude of the applied voltage and the piezoelectric strain constants (d_{31}) of the material, and is given by

$$\varepsilon_1^f = \frac{d_{31} \cdot V}{t_p} \tag{1}$$

where t_p is the thickness of the piezoelectric element. When a voltage is applied across a piezoelectric element which is bonded to a structure, it will attempt to expand/contract but will be constrained somewhat due to the stiffness of the beam.

When piezoactuators are activated, surface traction/compression is generated at the piezoactuator/beam interface. If the applied voltage varies sinusoidally with time, the substructure experiences harmonic excitation. Given a combined structure that is thin compared to the radius of curvature, a linear strain distribution can be assumed across the thickness direction [7] and therefore the strains at each of the interfaces will be continuous. The strain is given by

$$\varepsilon(z) = k \cdot z + \varepsilon_0 \tag{2}$$

where k is the strain slope and ε_0 is the intercept with the z axis as sketched in Figure 2.

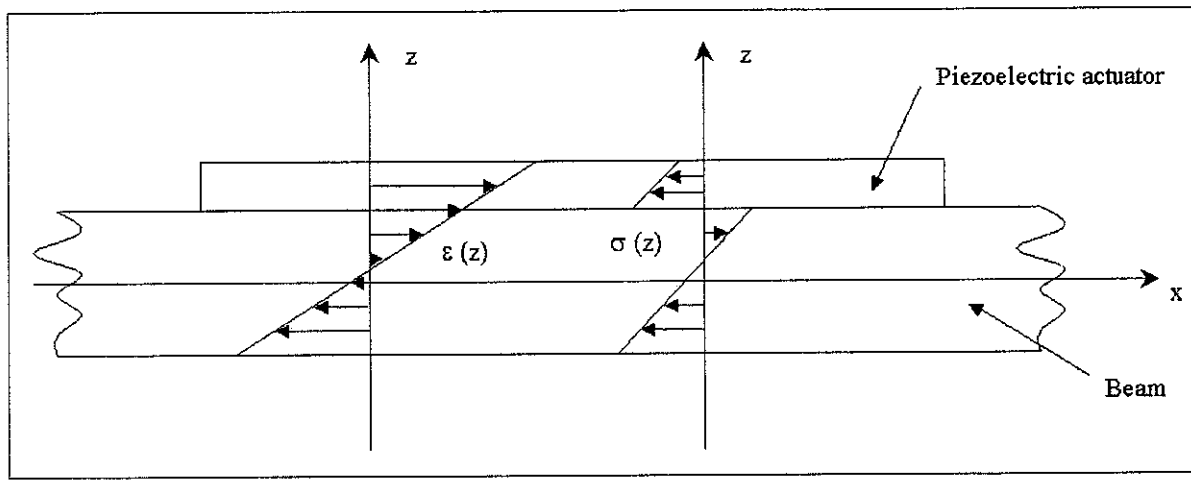

Figure 2 – Strain and stress distribution due to excitation of one piezoelectric actuator bonded to a beam

Note that if the piezoelectric element is forced to expand, a compressive state is induced in it due to the stiffening effect of the beam, while if it is forced to contract a tensile state is induced instead.

The deformation induced by the actuator to the beam underneath is equivalent to the superposition of a deformation induced by a pair of moments M_i and a deformation induced by a pair of forces F_i, as illustrated in Figure 3, which are given by

$$M_i = Y_b \cdot I_b \cdot k = C_2 \cdot Y_b \cdot I_b \cdot \frac{\varepsilon^f}{t_b/2} = K_2 \cdot \varepsilon^f \tag{3}$$

$$F_i = A_b \cdot Y_b \cdot \varepsilon_0 = C_3 \cdot Y_b \cdot A_b \cdot \varepsilon^f = K_3 \cdot \varepsilon^f \tag{4}$$

respectively, where C_2 and C_3 are constants given by:

$$C_2 = \frac{3 \cdot Y \cdot T \cdot (1+T)}{1+4 \cdot T \cdot Y + 6 \cdot T^2 \cdot Y + 4 \cdot T^3 \cdot Y + T^4 \cdot Y^2} \tag{5}$$

$$C_3 = \frac{Y \cdot T \cdot (1+T^3 \cdot Y)}{1+4 \cdot T \cdot Y + 6 \cdot T^2 \cdot Y + 4 \cdot T^3 \cdot Y + T^4 \cdot Y^2} \tag{6}$$

and the T is the thickness ratio and Y is the ratio of the Young's modulus of the piezoelectric element to the Young's modulus of the beam and are given by

$$T = \frac{t_p}{t_b} \qquad\qquad Y = \frac{Y_p}{Y_b} \tag{7.a, 7.b}$$

The subscripts b and p refer to the beam and piezoelectric element respectively.

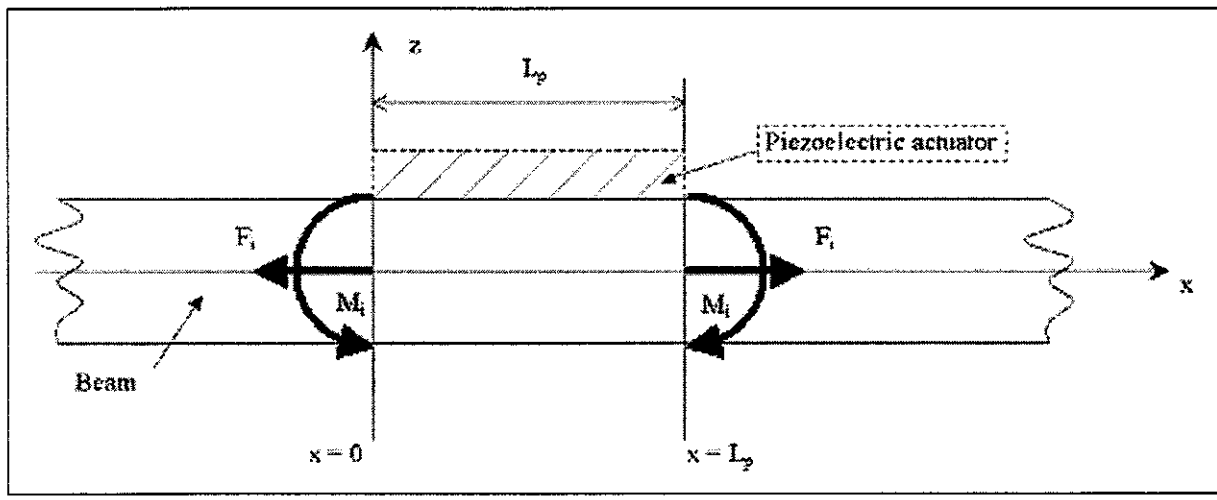

Figure 3 – Equivalent force and moment distributions

One of the main conclusions drawn in reference [6] is that there is an actuator/beam thickness ratio that maximizes the effective load. This depends on the actuator/beam Young's modulus ratio. To determine this, the strain ratio R is defined, which is the strain at the interface between the actuator and the beam divided by the free piezoactuator strain:

$$R = \frac{\varepsilon^s}{\varepsilon^f} = \frac{Y \cdot T \cdot (4+3 \cdot T + T^3 \cdot Y)}{1+4 \cdot T \cdot Y + 6 \cdot T^2 \cdot Y + 4 \cdot T^3 \cdot Y + T^4 \cdot Y^2} \tag{8}$$

This equation is plotted in Figure 4 for steel and aluminium beams as a function of the thickness ratio. As shown in Figure 4, there is an optimal thickness ratio for T less than one and it depends on the substructure material. It is also shown that the strain ratio tends to unity as the thickness ratio becomes very large. This is consistent with the fact that if the thickness of the piezoactuator is very

large compared to the beam thickness, the strain of the piezoelectric element will not be affected by the relatively light stiffening effect of the beam.

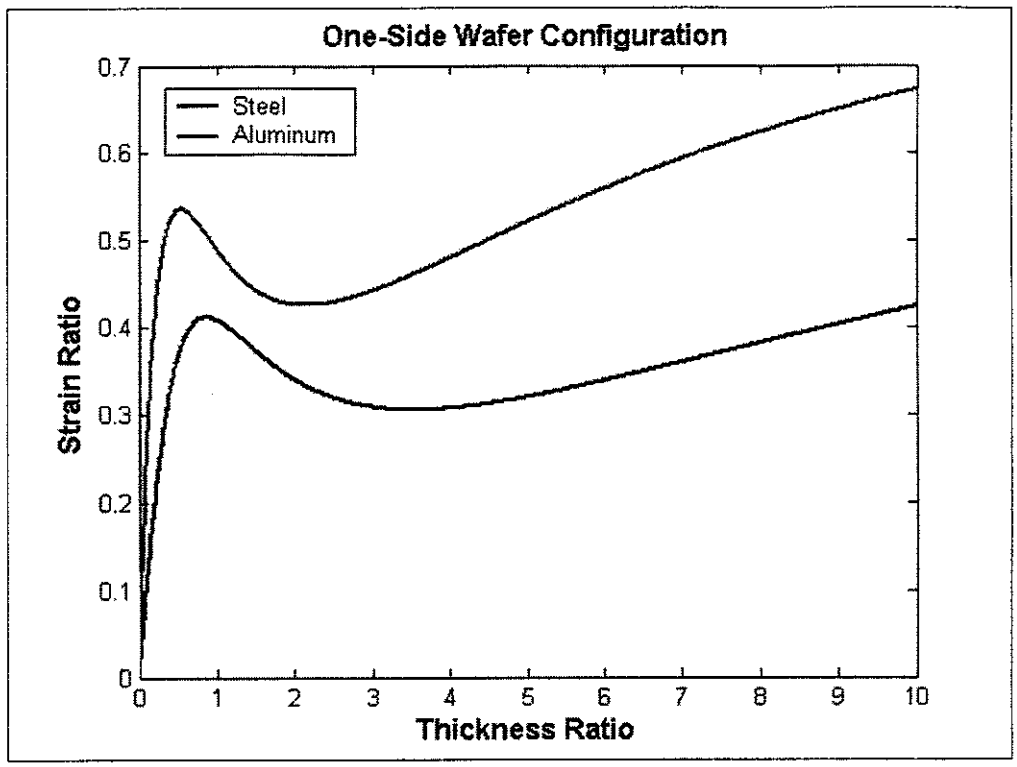

Figure 4 – Strain Ratio as a function of Thickness Ratio for one piezoelectric actuator

3 – System and Model Validation

The system studied is the simply supported aluminum beam illustrated in Figure 5, whose properties are given in Table 1.

Length (mm)	Width (mm)	Thickness (mm)	Young's Modulus (N/m^2)	Mass Density (kg/m^3)
395	25	5	7.1×10^{10}	2700

Table 1 – Beam properties

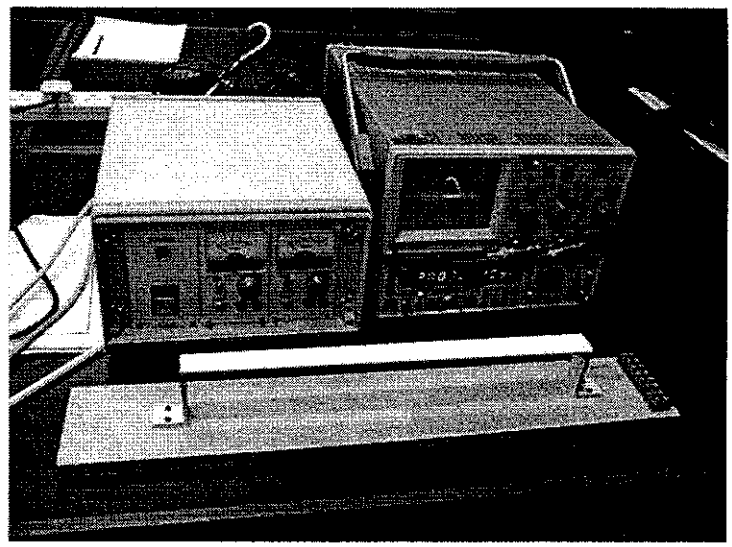

Figure 5 – Picture of the beam that was studied

In order to simulate the system and analyse its performances, a mathematical model of the system is needed. It was designed and built to behave as a simply-supported beam, whose mathematical model can be derived in simple analytical form. Particular care has thus been given to the construction of the physical supports for the beam, which can be seen in detail in Figure 6a. A simple support has the conditions of zero displacement and zero bending moment as shown in Figure 6b.

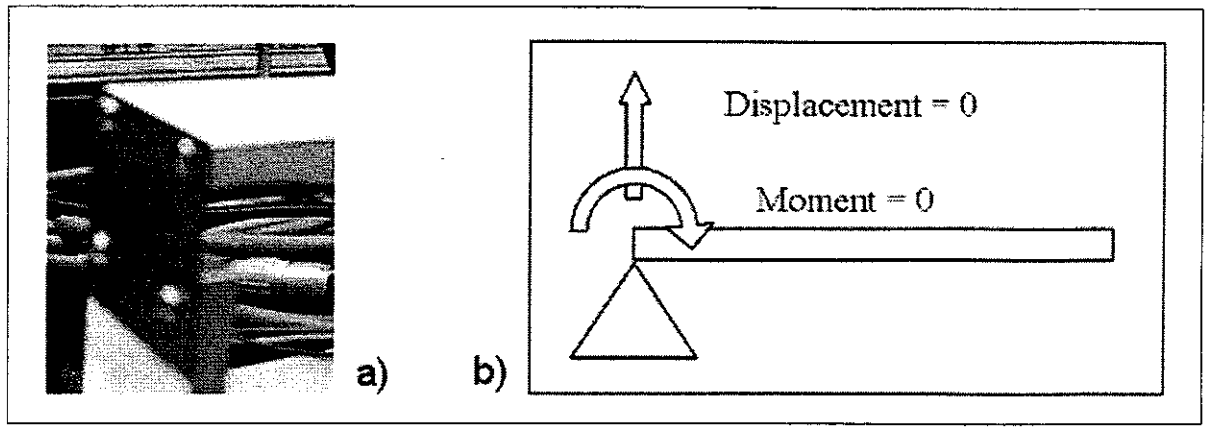

Figure 6 – Picture of the constraints on the beam, a) and Sketch of the boundary conditions, b)

An Euler-Bernoulli beam model was chosen to represent the physical system. The equation of motion is given by:

$$Y \cdot I \frac{\partial^4 w(x,t)}{\partial x^4} + \rho \cdot A \frac{\partial^2 w(x,t)}{\partial t^2} = p_d(x,t) \tag{9}$$

(A list of symbols is given at the beginning of the report). The boundary conditions are given by

$$\begin{cases} w(0,t) = w(L,t) = 0 & \text{(10.a)} \\ \dfrac{\partial^2 w(0,t)}{\partial x^2} = \dfrac{\partial^2 w(L,t)}{\partial x^2} = 0 & \text{(10.b)} \end{cases}$$

The out-of-plane displacement of any section along the beam can be estimated by the modal expansion approach, where the displacement is given by

$$w(x,t) = \sum_{n=1}^{\infty} q_n(t) \cdot \phi_n(x) \tag{11}$$

and q_n are the modal amplitudes and ϕ_n are the mode shapes. For harmonic motion, this transforms in the frequency domain to

$$W(x,\omega) = \sum_{n=1}^{\infty} q_n(\omega) \cdot \phi_n(x) \tag{12}$$

$$q_n(\omega) = \frac{\int_0^L \left[p_d(x,\omega) \cdot \phi_n(x) + m_d(x,\omega) \cdot \phi_n'(x) \right] \cdot dx}{M_n \cdot \left[\omega_n^2 \cdot (1 + j\eta) - \omega^2 \right]} \tag{13}$$

where $p_d(x, \omega)$ and $m_d(x, \omega)$ are the force and moment distribution acting on the beam respectively. The mode shapes, natural frequencies and generalized mass for the simply-supported beam are respectively given by

$$\phi_n(x) = \sqrt{2} \cdot \sin\left(\frac{n \cdot \pi}{l} \cdot x \right) \tag{14}$$

$$\omega_n = \left(\frac{n \cdot \pi}{l} \right)^2 \cdot \sqrt{\frac{Y_b \cdot I_b}{\rho_b \cdot A_b}} \tag{15}$$

$$M_n = M_b \tag{16}$$

being M_b the mass of the beam.

Once a theoretical model has been developed, it is prudent to validate it by experimental tests on a real structure. For this purpose, mode shapes and frequency response functions (FRF) are chosen for comparison.

A piezoelectric actuator, whose properties are given in Table 2, was bonded on the beam surface at 100.5 mm from the right edge of the beam, as illustrated in Figures 7 and 8. It acted as primary excitation, exerting a pair of moments located at its edges [7] and thus setting the beam into out-of-plane vibration. In-plane vibrations, caused by the longitudinal forces coupled to the moments, are neglected in this first derivation.

Length (mm)	Width (mm)	Thickness (mm)	Young's Modulus (N/m^2)	Dielectric Constant ($m\ V^{-1}$)
25	25	1	6×10^{10}	212×10^{-12}

Table 2 – Piezoelectric actuator (PZT) properties

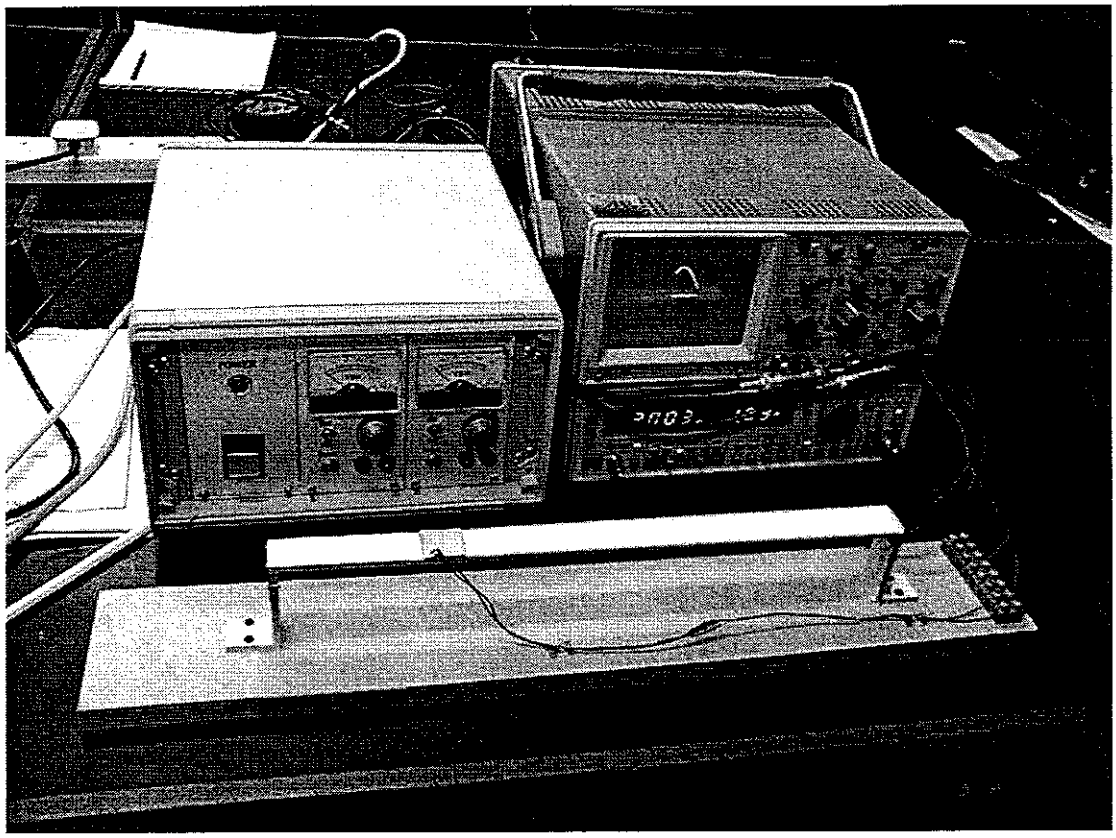

Figure 7 – Picture of the beam and the primary piezoactuator

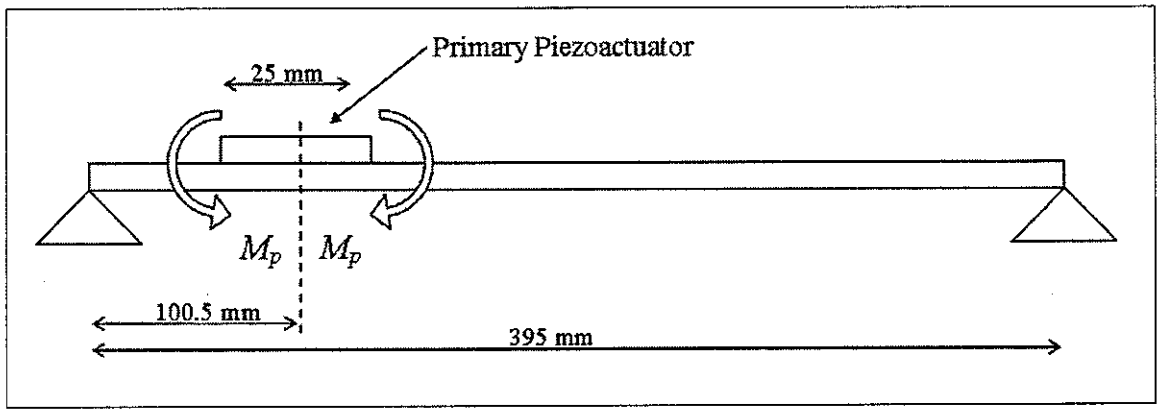

Figure 8 – Sketch of the beam and the primary piezoactuator

For this particular type of excitation the modal amplitude from Eq. 13 is given by:

$$q_n(\omega) = \frac{M_P \cdot \left[\phi_n'\left(x_P - \frac{d}{2}\right) - \phi_n'\left(x_P + \frac{d}{2}\right)\right]}{M_n \cdot \left[\omega_n^2 \cdot (1 + j\eta) - \omega^2\right]} \tag{17}$$

The out-of-plane displacement at any section along the beam for unitary excitation moment pair, i.e. the receptance, is derived from Eq. 14 and is given by:

$$R_{wP} = R(x_w, x_P) = \frac{W(x_w)}{M_P} = \sum_{n=1}^{\infty} \frac{\phi_n(x_w)}{M_n \cdot \left[\omega_n^2 \cdot (1 + j\eta) - \omega^2\right]} \cdot \left[\phi_n'\left(x_P - \frac{d}{2}\right) - \phi_n'\left(x_P + \frac{d}{2}\right)\right] \tag{18}$$

The out-of-plane velocity at any section along the beam for excitation by a single moment pair, i.e. the mobility, is given by

$$Y(x_w, x_P) = j\omega \cdot R(x_w, x_P) \tag{19}$$

The beam is discretized into 13 elements, each element being identified by its centre. The magnitude and phase of the mobility at each point on the beam is calculated using equations (18) and (19) and compared to the measured mobilities, which were measured using a laser vibrometer as illustrated in Figure 9.

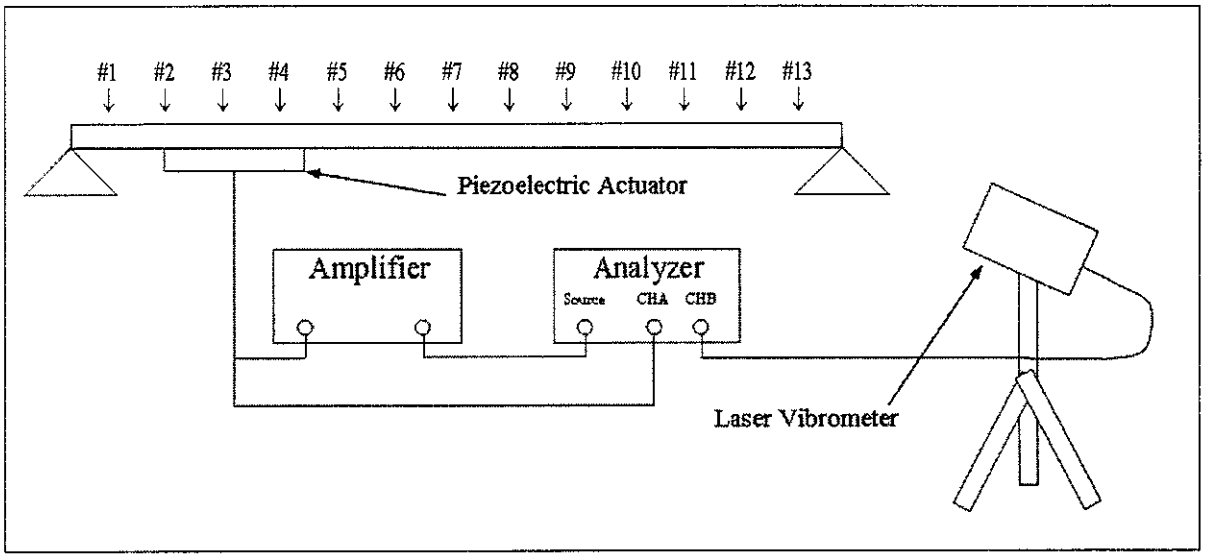

Figure 9 – Experiment Setup

Experimental mobilities are measured in m/Volts. In order to compare these with the theoretical quantities (m/Nm), the theoretical mobilities are multiplied by a constant factor C_p, which takes into account the electromechanical characteristics of the piezoelectric actuator. This factor, which represents the piezoelectric actuator transfer function, is calculated by rearranging Eq. 3 to give

$$C_p = C_2 \cdot Y_b \cdot \frac{I_b}{t_b/2} \cdot \frac{d_{31}}{t_p} \tag{20}$$

Figures 10, 11 and 12 show the comparison of the simulated and experimental mobility at three different points along the beam (refer to Figure 9 for points identification).

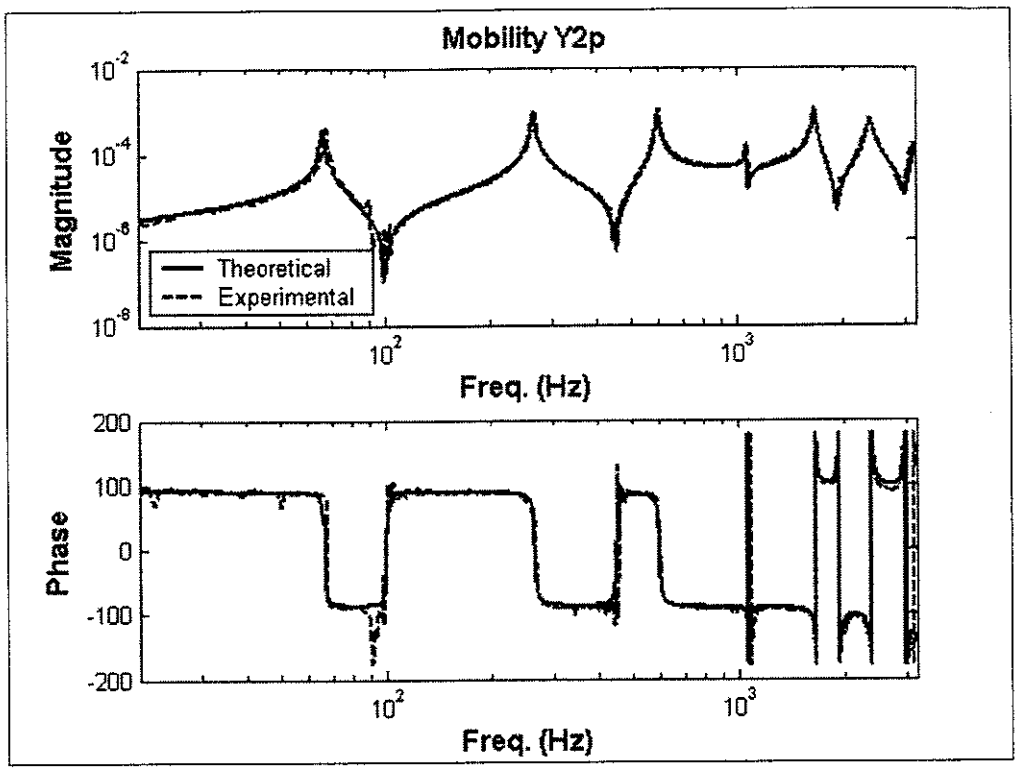

Figure 10 – Mobility at point #2

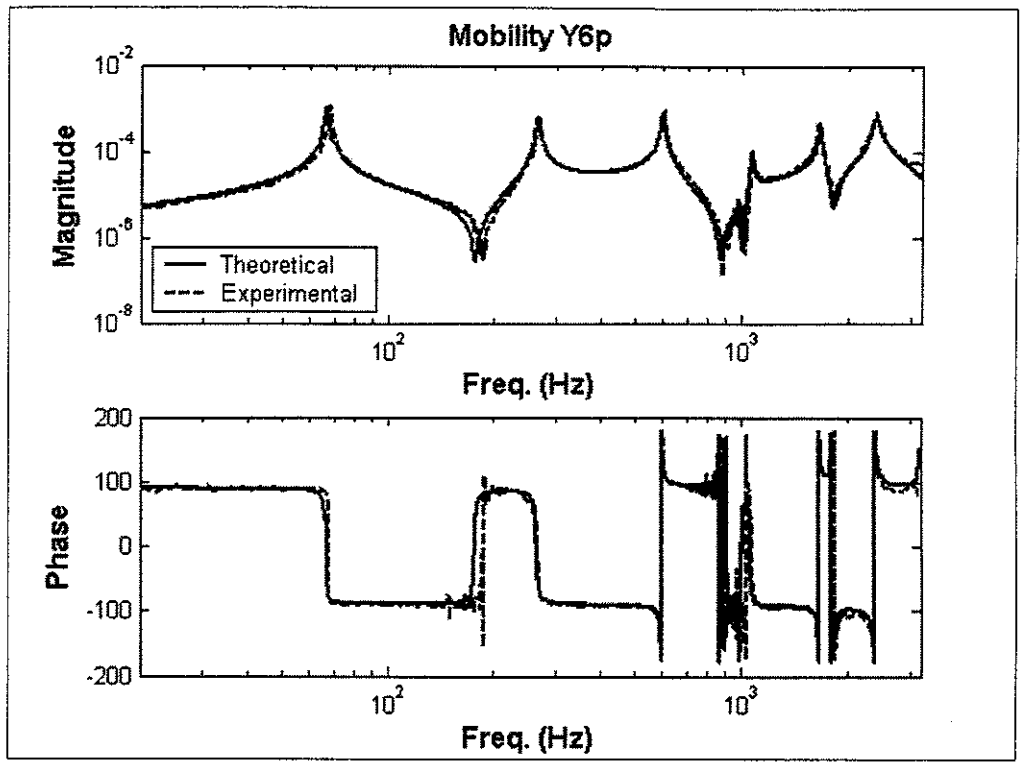

Figure 11 – Mobility at point #6

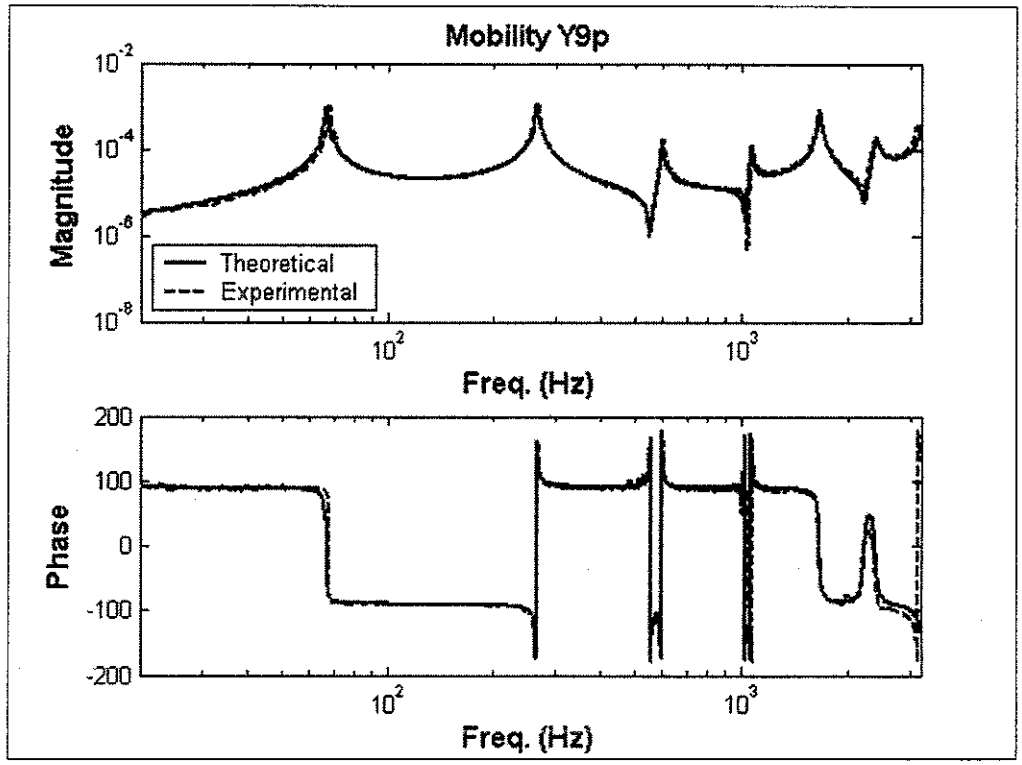

Figure 12 – Mobility at point #9

From the measured mobilities it is also possible to estimate the damping in the beam, which is mainly effected by the joints at its extremes since the aluminium beam itself has very low structural damping estimated to be about 0.005.

The first four natural frequencies were identified experimentally and the corresponding mode shapes were estimated by measuring the out-of-plane displacement at all the 13 points along the beam due to a constant excitation of arbitrary amplitude. The mode shapes were then normalized so that the maximum value was equal to 1. Figures 13 to 16 show a comparison between the first four theoretical and experimentally determined mode shapes.

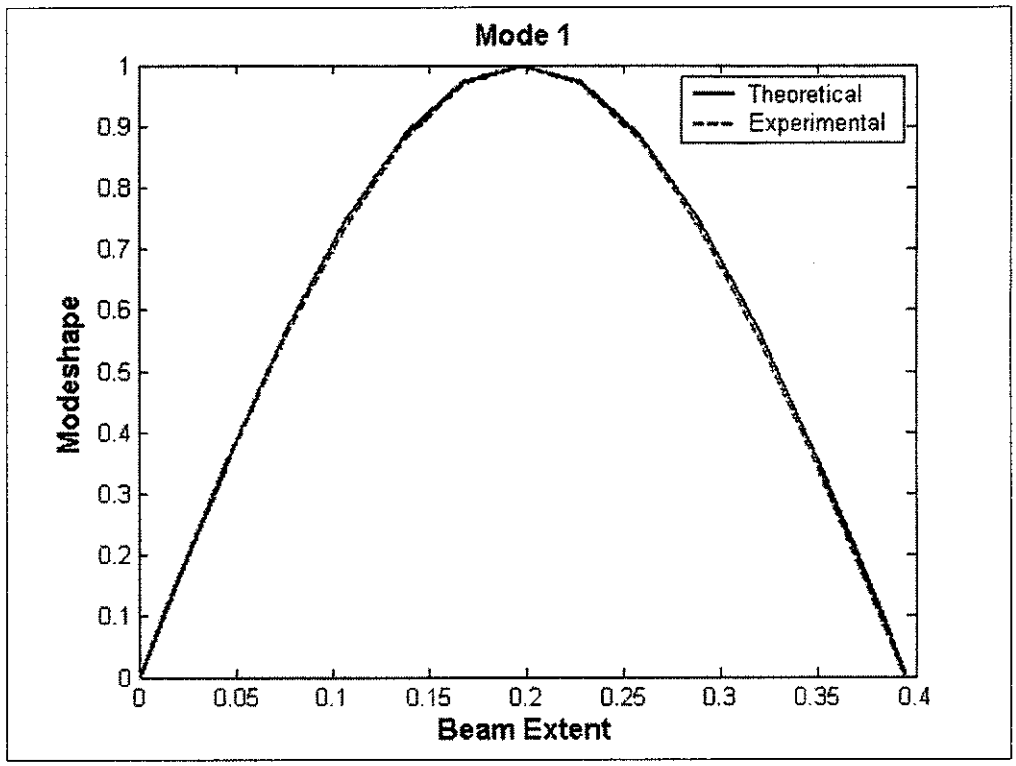

Figure 13 – First Mode Shape

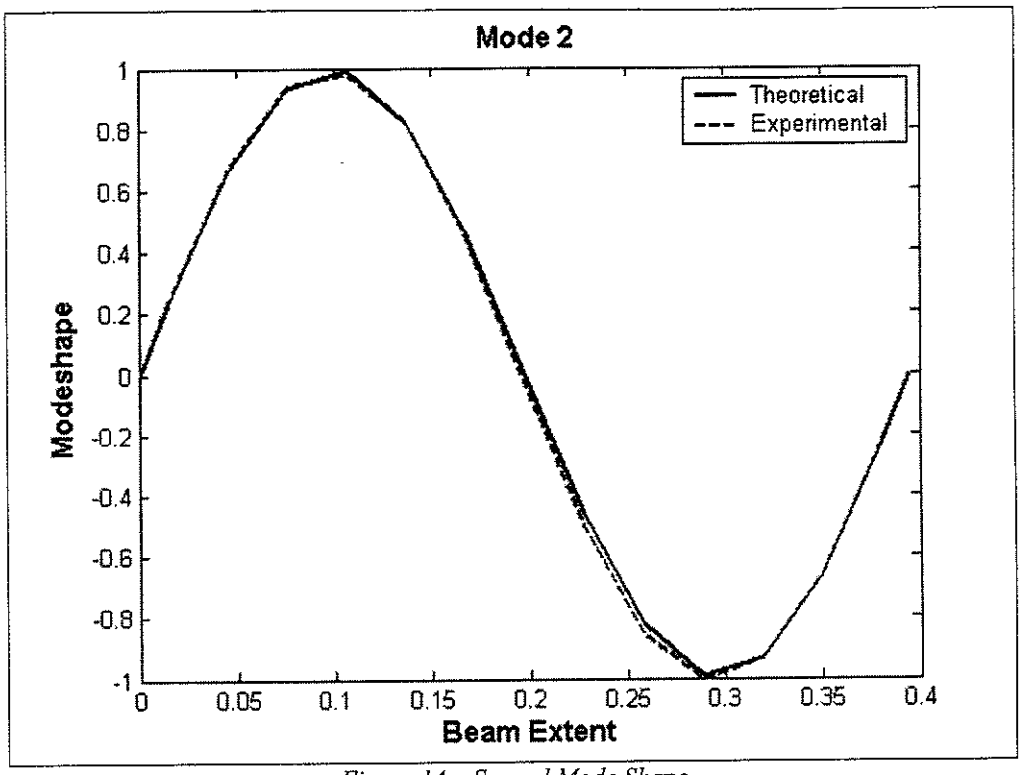

Figure 14 – Second Mode Shape

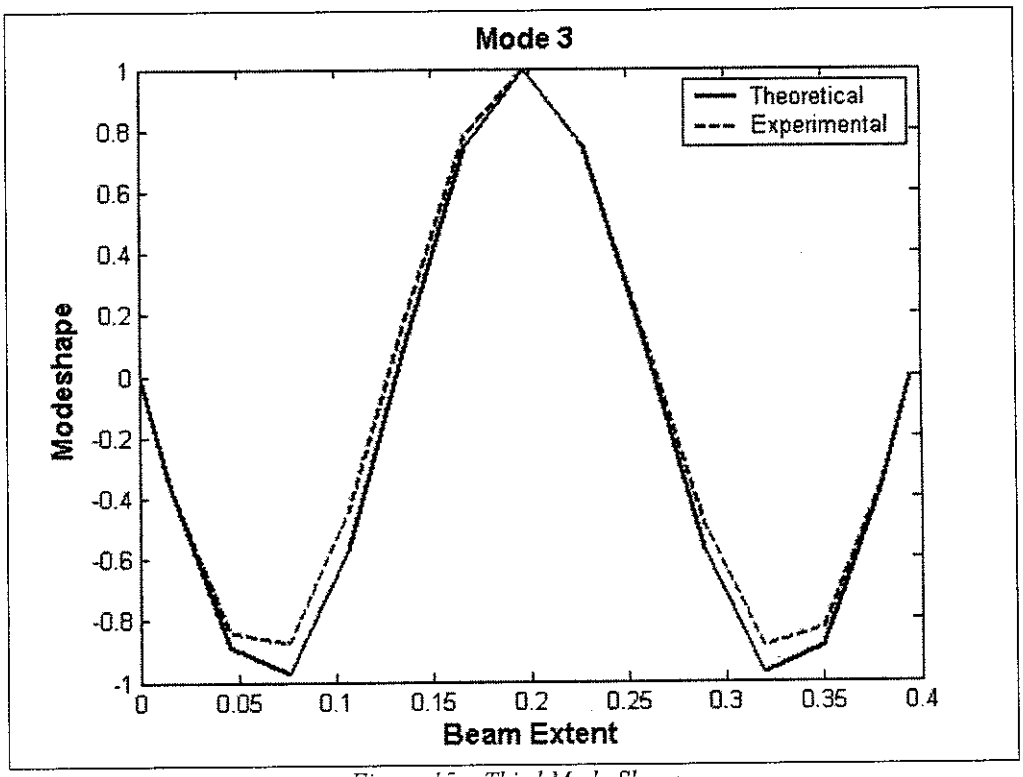

Figure 15 – Third Mode Shape

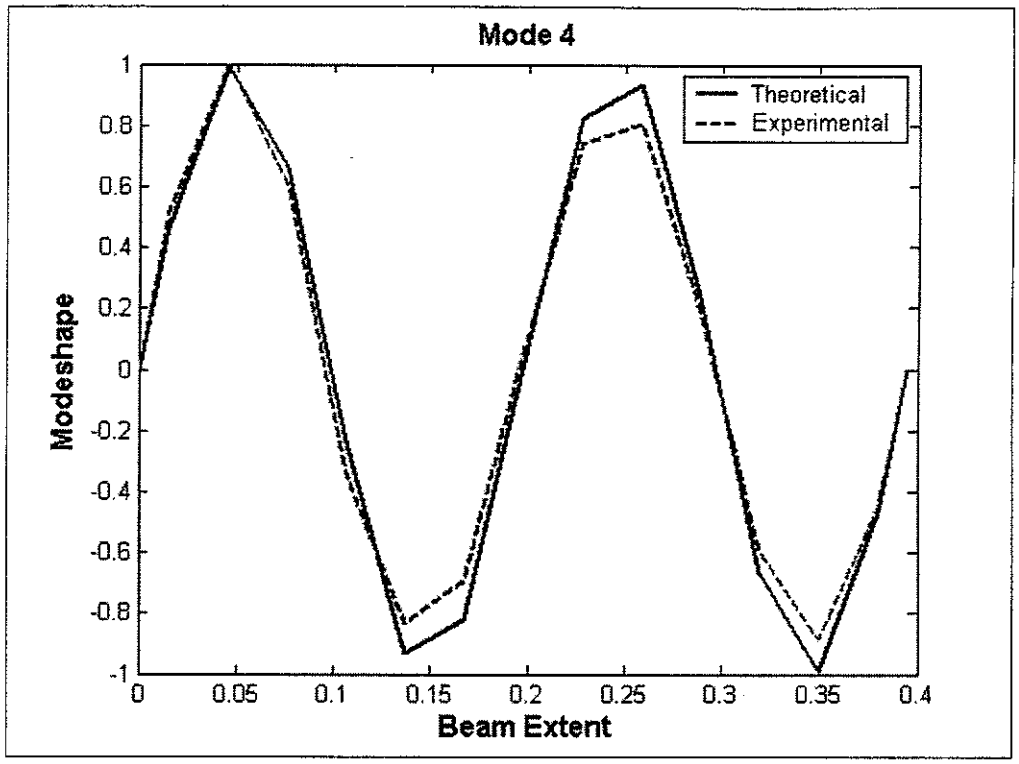

Figure 16 – Fourth Mode Shape

As shown by the comparison of the theoretical and measured mobilities, and mode shapes, the theoretical model seems to be a reasonable representation of the beam. Thus this model is used as a mathematical model of the structure in this report.

4 – Global Vibration of a Beam

The global vibrational kinetic energy of the beam is given by

$$VKE(t) = \frac{1}{2}\int_0^L \dot{w}^2(x,t)\cdot m(x)\cdot dx \tag{21}$$

Where *m(x)* is beam mass distribution per unit length.

The time-averaged global vibrational kinetic energy of the beam is given by [8]:

$$VKE(\omega) = \frac{1}{4}\int_0^L \left|V(x,\omega)\right|^2 \cdot m(x)\cdot dx = \frac{1}{4}\omega^2 \sum_n M_n \cdot q_n^2(\omega) \tag{22}$$

which depends only on the modal amplitudes of the system.

From an experimental point of view, the time-averaged global vibrational kinetic energy of the beam is estimated by dividing the beam into *p* elements of finite length and measuring the transverse velocity at their middle point, assuming that is the velocity of the element. The kinetic energy is thus estimated as the sum of the kinetic energy of each element, according to the following expression:

$$VKE(\omega) \cong \frac{1}{4}\sum_{e=1}^{p} m_e \cdot V(x_e,\omega)\cdot V^*(x_e,\omega) = \frac{1}{4} {M_P}^2 \sum_{e=1}^{p} m_e \cdot Y(x_e,\omega)\cdot Y^*(x_e,\omega) \tag{23}$$

Figure 17 shows a comparison of the experimental and theoretical results.

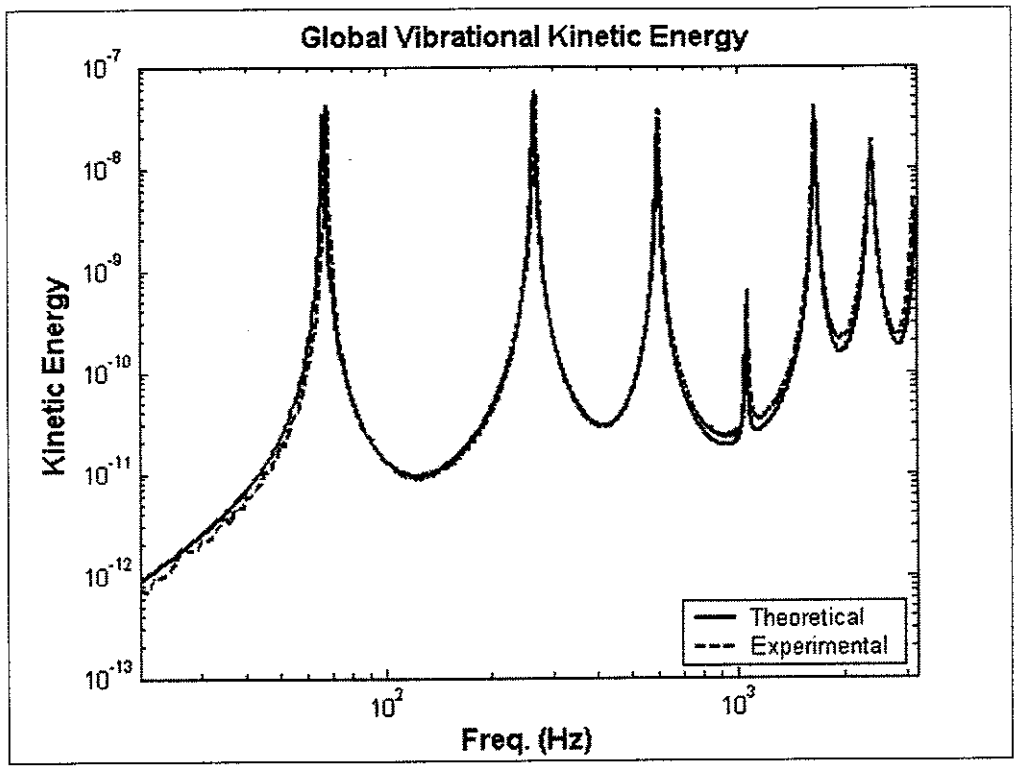

Figure 17 – Theoretical and experimental vibrational kinetic energy of a simply supported beam excited by a single piezoelectric actuator

5 – The System used to Study the Active Control Algorithms

In this section the performance of the control system is investigated in terms of vibrational kinetic energy reduction. In order to attenuate the vibrations induced in the beam by the primary piezoelectric actuator, a secondary piezoelectric actuator in employed and thus bonded on the beam at 94.5mm from its left end, as illustrated in Figure 18 and sketched in Figure 19. The vibration induced by this latter source will interfere with the primary vibration actively damping the overall system.

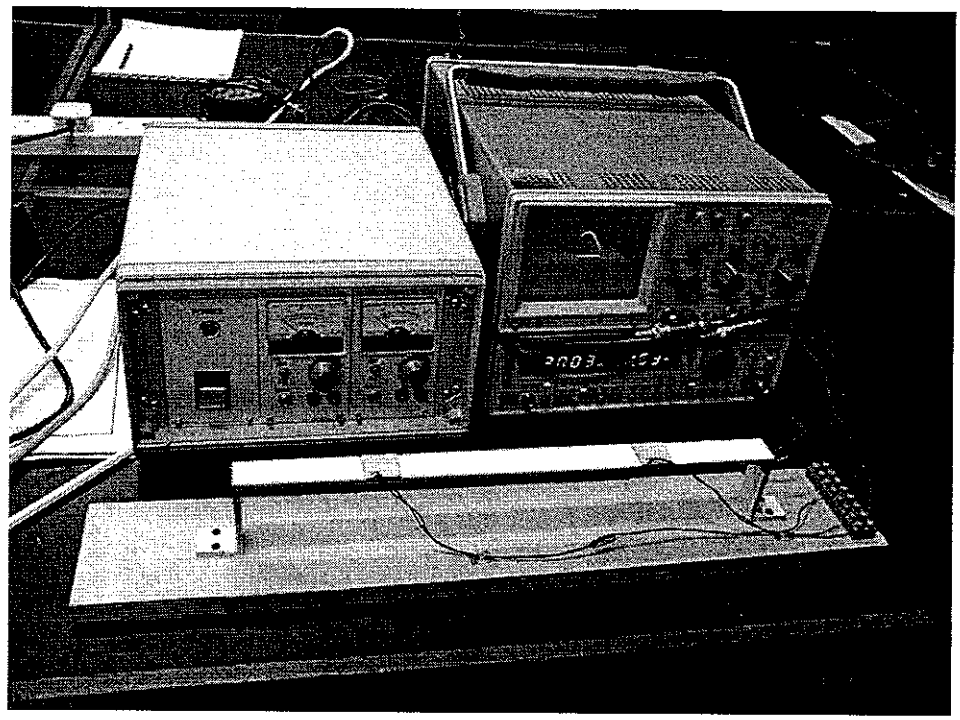

Figure 18 – Picture of the beam and the primary and secondary piezoactuators

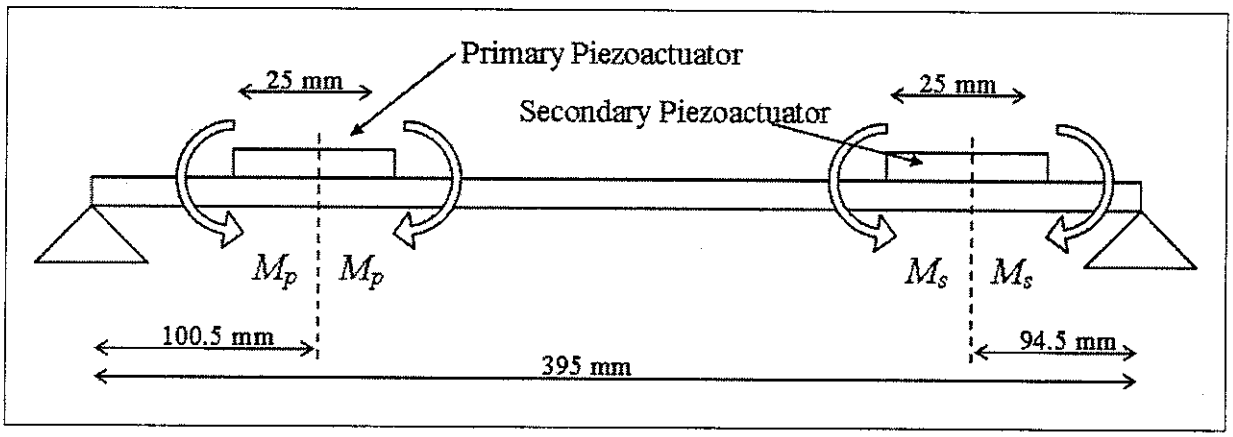

Figure 19 – Sketch of the beam and the primary and secondary piezoactuators

The following sections describe the study and analysis of the Feedforward and Velocity Feedback control strategies separately.

6 – FeedForward Strategy

A feedforward control strategy is effective when the structure to be controlled is excited by a primary excitation at a single frequency. Figure 20 shows such a control system as a block diagram. Figure 21 is a sketch of the actual system.

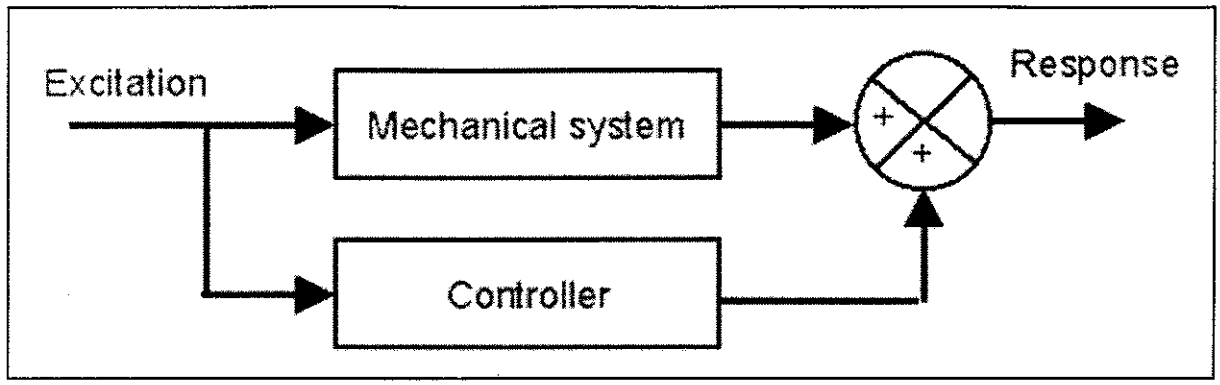

Figure 20 – Block Diagram of a Feedforward Control System

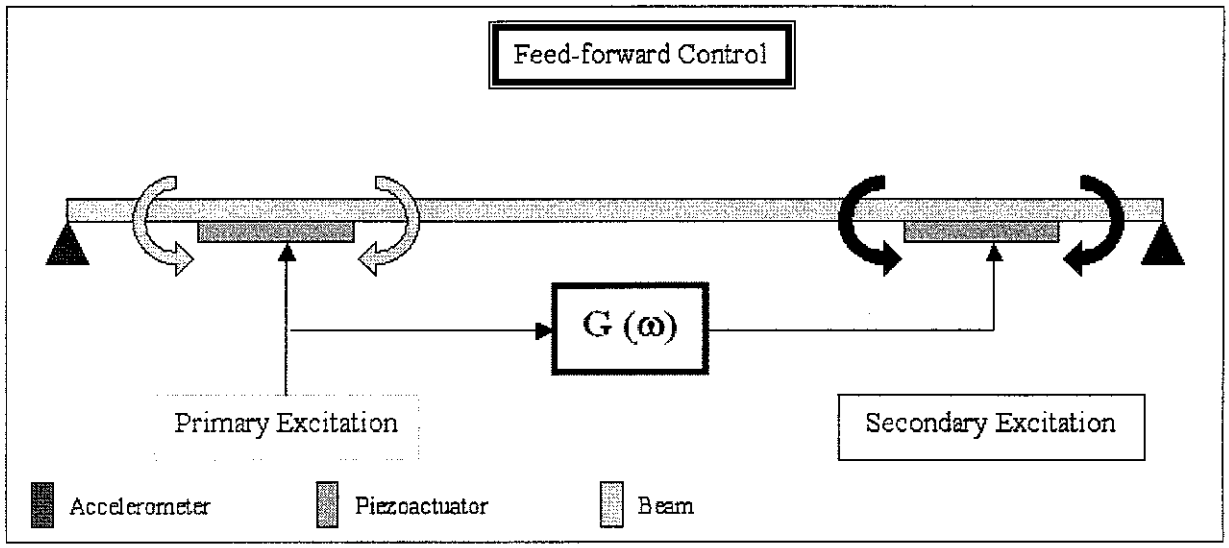

Figure 21 – Sketch of the FeedForward Control System

The aim is to design a controller $G(\omega)$ such that the global vibrational kinetic energy of the beam is minimized for each given frequency of the primary excitation.

6.1 – Theoretical Simulation

The modal expansion of the transverse displacement at some point on the beam (Eq. 13) is first expressed as a vector inner product

$$W(x,\omega) = \mathbf{q}^T(\omega) \circ \boldsymbol{\varphi}(x) \tag{24}$$

where:

$$\mathbf{q}^T(\omega) = \{q_1(\omega), q_2(\omega), ..., q_n(\omega)\} \tag{25.a}$$

$$\boldsymbol{\varphi}^T(x) = \{\phi_1(x), \phi_2(x), ..., \phi_n(x)\} \tag{25.b}$$

The global vibrational kinetic energy of the beam given by Eq. 22, can then be written as

$$VKE(\omega) = \frac{M_b \cdot \omega^2}{4} \mathbf{q}^H(\omega) \circ \mathbf{q}(\omega) \tag{26}$$

Since the beam is excited by two moment pairs, M_P and M_S, where:

$$M_s = G(\omega) \cdot M_p \tag{27}$$

The vector of structural mode amplitudes $\mathbf{q}(\omega)$ is the superposition of components $\mathbf{q_P}(\omega)$ due to the primary source M_P and those $\mathbf{q_S}(\omega)$ due to the secondary source M_S, weighted by the controller $G(\omega)$, so that in general:

$$\mathbf{q}(\omega) = \mathbf{q_p}(\omega) + \mathbf{q_s}(\omega) \cdot G(\omega) \tag{28}$$

Where:

$$\mathbf{q_p}^T(\omega) = \{q_{p1}(\omega), q_{p2}(\omega), ..., q_{pn}(\omega)\} \tag{29}$$

$$q_{pn}(\omega) = \frac{M_p \cdot \left[\phi_n'\left(x_P - \frac{d}{2}\right) - \phi_n'\left(x_P + \frac{d}{2}\right)\right]}{M_n \cdot \left[\omega_n^2 \cdot (1 + j\eta) - \omega^2\right]} \tag{30}$$

$$\mathbf{q_s}^T(\omega) = \{q_{s1}(\omega), q_{s2}(\omega), ..., q_{sn}(\omega)\} \tag{31}$$

$$q_{sn}(\omega) = \frac{M_p \cdot \left[\phi_n'\left(x_S - \frac{d}{2}\right) - \phi_n'\left(x_S + \frac{d}{2}\right)\right]}{M_n \cdot \left[\omega_n^2 \cdot (1 + j\eta) - \omega^2\right]} \tag{32}$$

The global vibrational kinetic energy can thus be written in the standard Hermitian quadratic form as:

$$VKE(\omega)=\frac{M_b\omega^2}{4}\left[G^H\cdot\mathbf{q}_s{}^H\circ\mathbf{q}_s\cdot G+G^H\cdot\mathbf{q}_s{}^H\circ\mathbf{q}_p+\mathbf{q}_p{}^H\circ\mathbf{q}_s\cdot G+\mathbf{q}_p{}^H\circ\mathbf{q}_p\right] \tag{33}$$

VKE(ω) is thus a quadratic function in *G(ω)*, which is guaranteed to have a minimum value for a value of *G(ω)* given by [8]:

$$G_{opt}(\omega)=-\left[\mathbf{q}_s{}^H\circ\mathbf{q}_s\right]^{-1}\circ\mathbf{q}_s{}^H\circ\mathbf{q}_p \tag{34}$$

with a corresponding minimum value of *VKE(ω)* given by:

$$VKE_{opt}(\omega)=\frac{M_b\omega^2}{4}\mathbf{q}_p{}^H\circ\left[\mathbf{I}-\mathbf{q}_s\circ\left[\mathbf{q}_s{}^H\mathbf{q}_s\right]^{-1}\circ\mathbf{q}_s{}^H\right]\circ\mathbf{q}_p \tag{35}$$

Figure 22 shows the uncontrolled and optimally controlled kinetic energy. Figure 23 shows the Frequency response function (FRF) of the optimal controller.

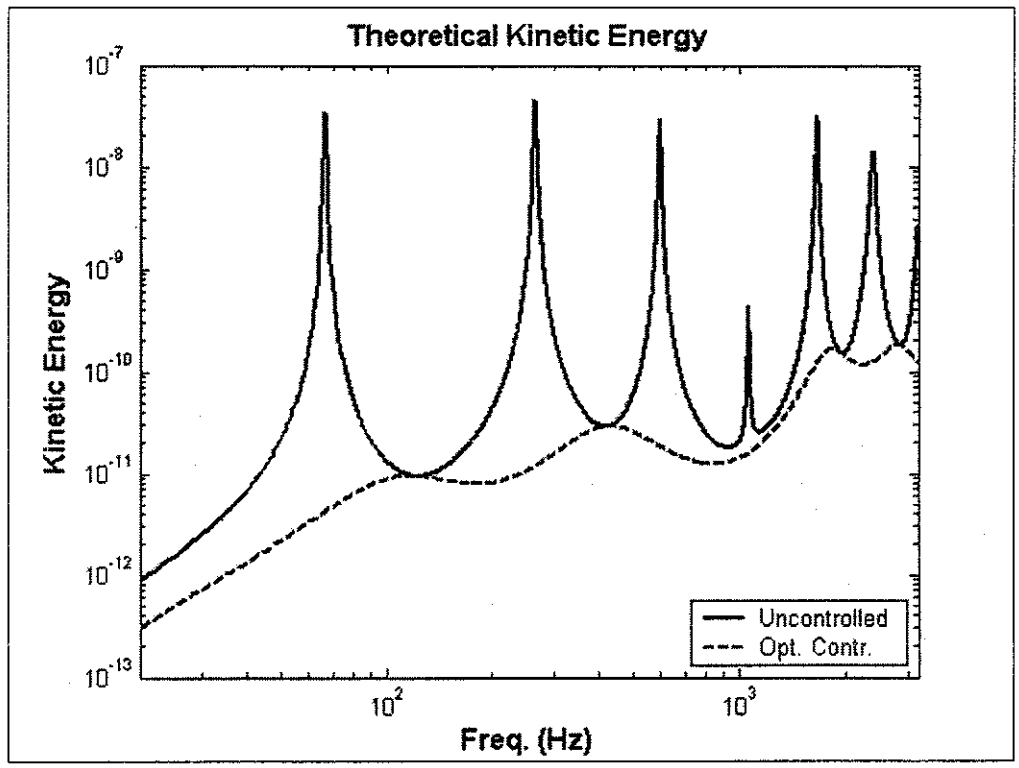

Figure 22 – Uncontrolled and optimally controlled global VKE (Theoretical Simulation)

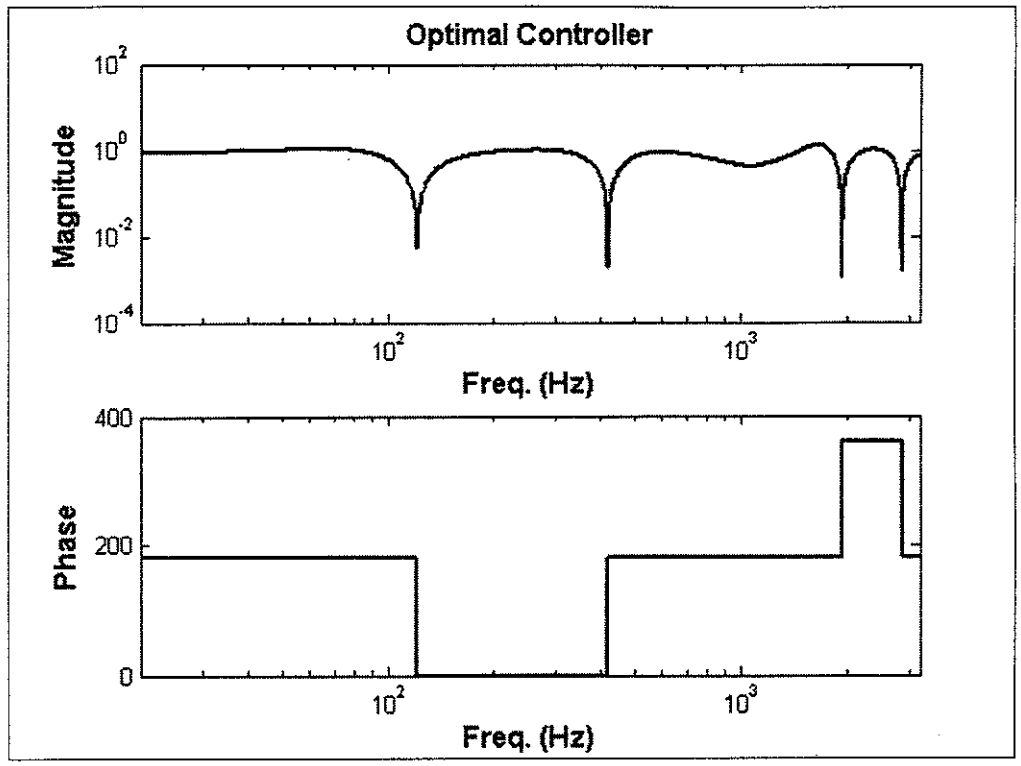

Figure 23 – FRF of the Optimal Controller (Theoretical Simulation)

As can be seen from Figure 23 the theoretical controller is a real number, either in-phase or out-of-phase with the primary excitation. By comparing Figure 22 and Figure 23, one can also notice that it is particularly effective in the frequency bands where only one mode is dominant. In the frequency regions where two modes are dominant, the controller is less and less effective: at some frequencies the controlled and uncontrolled kinetic energy become similar and the best the controller can do is actually doing nothing.

6.2 – Experimental Off-Line Simulation

The optimized global vibrational kinetic energy of the beam and the controller FRF may be estimated starting from Eq. 23:

$$VKE(\omega) \cong \frac{1}{2}\sum_{e=1}^{p} m_e \cdot V(x_e,\omega)\cdot V^*(x_e,\omega) = \frac{1}{2} {M_P}^2 \sum_{e=1}^{p} m_e \cdot Y(x_e,\omega)\cdot Y^*(x_e,\omega) \tag{23}$$

where the mobility is now given as the superposition of the two components due to the primary and secondary excitation, as:

$$Y(x_e,\omega)=Y_p(x_e,\omega)+G(\omega)Y_s(x_e,\omega) \tag{36}$$

Substituting Eq. 36 into Eq.23, one gets the cost function $J(\omega)$, whose minimum is sought:

$$J(\omega)=\sum_{e=1}^{p}Y_{ep}{}^{H}Y_{ep}+G^{H}G\cdot\sum_{e=1}^{p}Y_{es}{}^{H}Y_{es}+G\cdot\sum_{e=1}^{p}Y_{ep}{}^{H}Y_{es}+G^{H}\cdot\sum_{e=1}^{p}Y_{es}{}^{H}Y_{ep} \tag{37}$$

Differentiating Eq.37 with respect to the real and imaginary part of $G(\omega)$, and setting the resulting expressions to zero and solving for $Re(G)$ and $Im(G)$ gives

$$\mathrm{Re}(G_{opt})=-\frac{\sum_{e=1}^{p}Y_{ep}{}^{H}Y_{es}+\sum_{e=1}^{p}Y_{es}{}^{H}Y_{ep}}{2\sum_{e=1}^{p}Y_{es}{}^{H}Y_{es}} \tag{38.a}$$

$$\mathrm{Im}(G_{opt})=-j\frac{\sum_{e=1}^{p}Y_{ep}{}^{H}Y_{es}-\sum_{e=1}^{p}Y_{es}{}^{H}Y_{ep}}{2\sum_{e=1}^{p}Y_{es}{}^{H}Y_{es}} \tag{38.b}$$

which is the optimal controller transfer function:

$$G_{opt}(\omega)=-\frac{\sum_{e=1}^{p}Y_{es}{}^{H}Y_{ep}}{\sum_{e=1}^{p}Y_{es}{}^{H}Y_{es}} \tag{39}$$

Substituting this expression for $G(\omega)$ into Eq.36 and combining this with Eq.23, gives the optimised global vibrational kinetic energy of the beam. Figure 24 shows the uncontrolled and optimally controlled kinetic energy by off-line simulation. Figure 25 shows the FRF of the optimal controller.

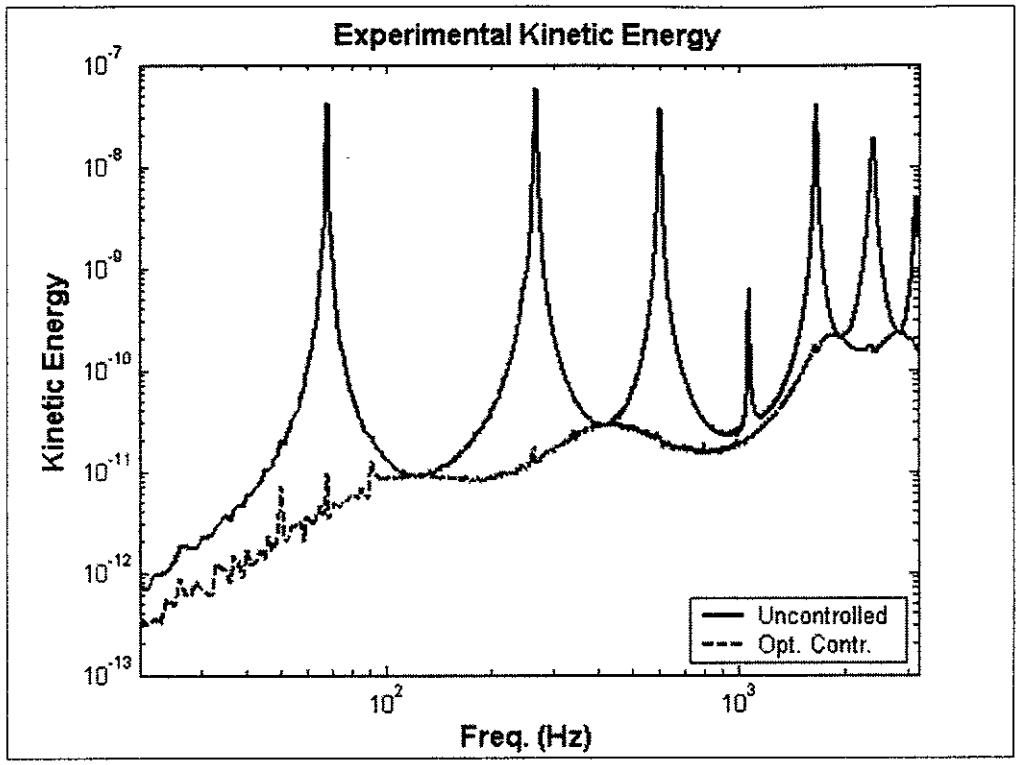

Figure 24 – Uncontrolled and optimally controlled global VKE (Off-Line Simulation)

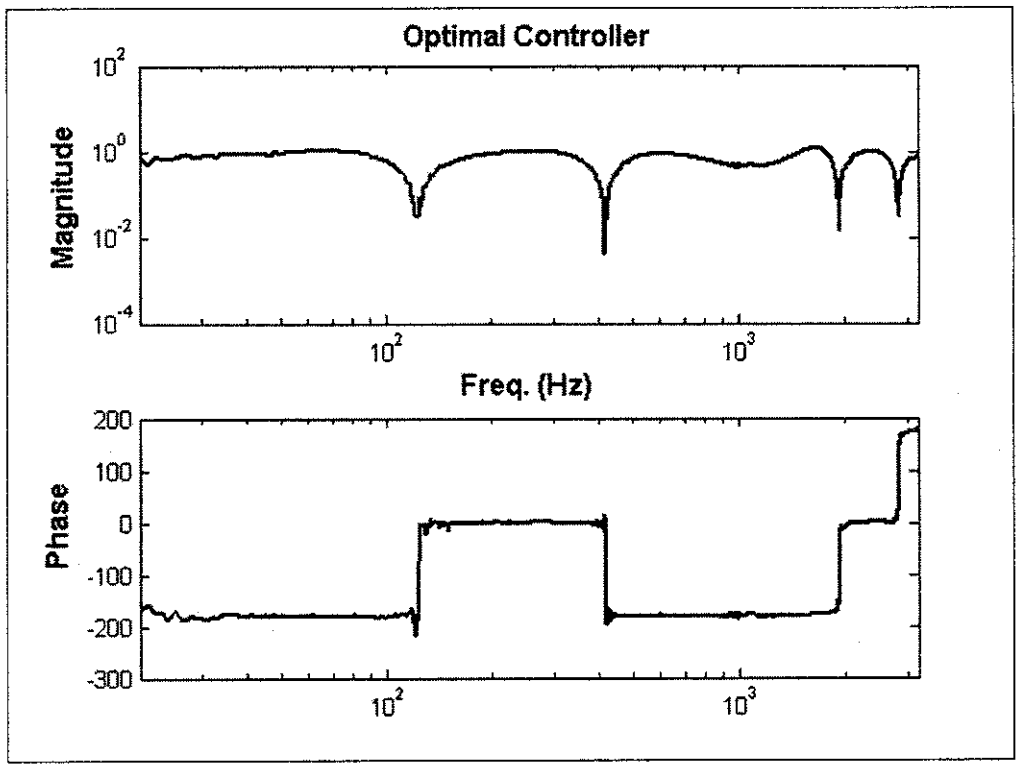

Figure 25 – Optimal Controller FRF (Off-Line Simulation)

In Figure 26 the FRFs of the controllers shown in Figure 23 and Figure 25 are plotted so that the theoretical and the off-line simulated results can be compared. A good agreement is clearly shown.

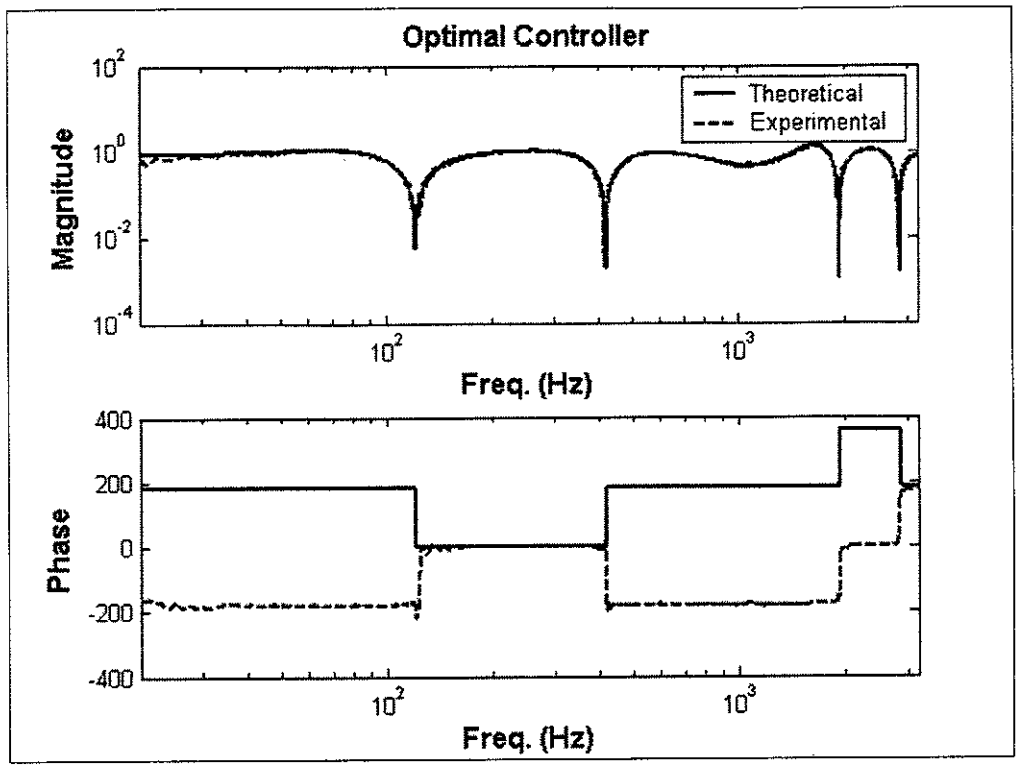

Figure 26 – Optimal Controller FRF (Theoretical and Off-Line Simulation)

7 – Direct Velocity Feedback Strategy

Feedback control strategy is effective when the structure to be controlled is excited by a primary random excitation. Figure 27 shows a block diagram of such a control system. Figure 28 is a sketch of the actual system, where, in particular, Direct Velocity Feedback (DVFB) with a velocity sensor/moment pair is applied.

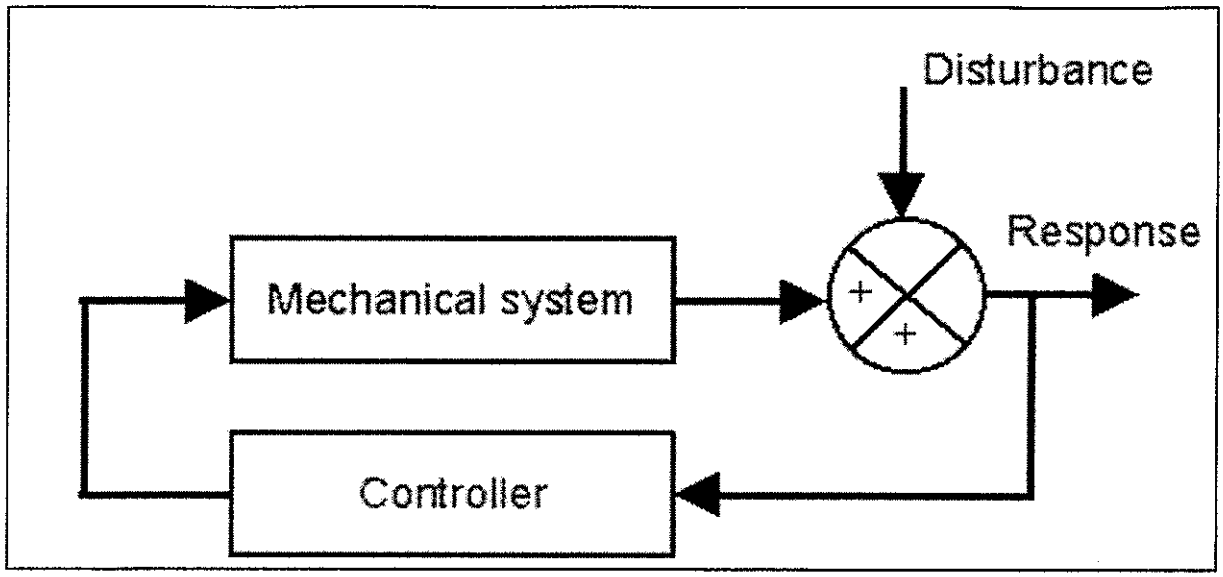

Figure 27 – Block Diagram of a Feedback Control System

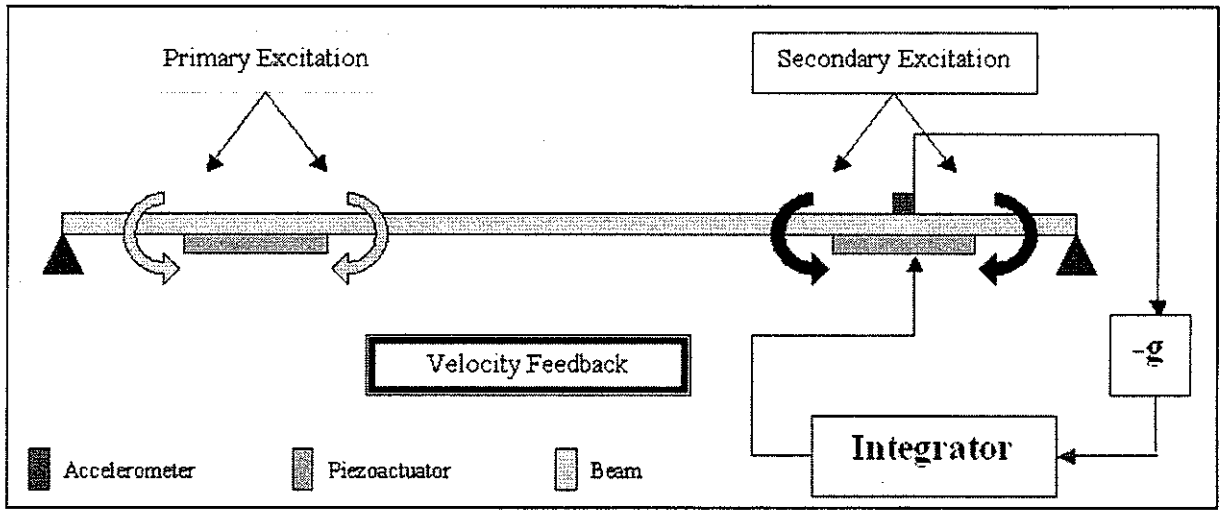

Figure 28 – Sketch of the Direct Velocity Feedback Control System

The vibration of the beam excited by a primary moment pair, M_P, is sensed by an accelerometer, whose signal is integrated and amplified with a negative feedback gain, $-g$, before supplied to a secondary moment pair, M_S.

The aim of the DVFB control approach is to find the optimum feedback gain g, in order to minimize the global vibrational kinetic energy of the beam in a given bandwidth. Stability is also an issue when a non-collocated velocity sensor/moment pair is used [9]. It is found that there is a limitation on the feedback gain due to stability requirements.

7.1 – Theoretical Simulation

The cost-function to be minimized in this case, is the integral of the global vibrational kinetic energy over the given bandwidth, which is chosen to be 0-3200 Hz.

$$J = \int_{\omega_b} VKE(\omega) d\omega \tag{40}$$

Figure 29 illustrates the graphical meaning of J.

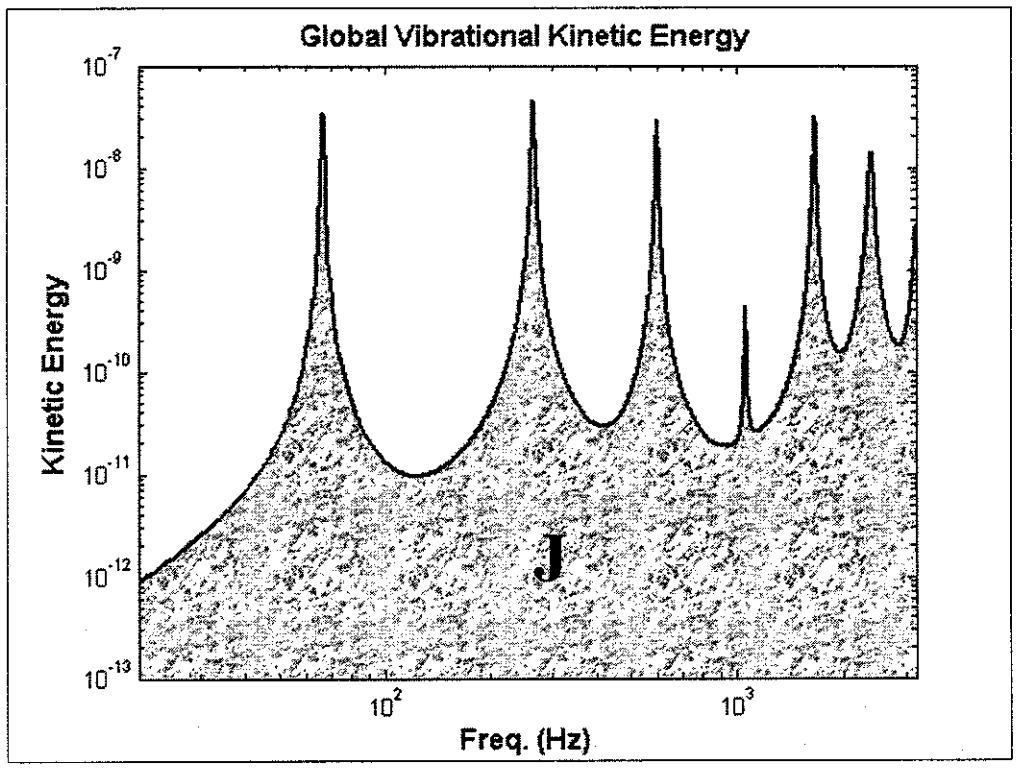

Figure 29 – Illustration of the cost-function J over a frequency band of 0-3.2 kHz

The global vibrational kinetic energy is again calculated using Eq.26. The beam is excited by two moment pairs, M_P and M_S, where now

$$M_s = -g \cdot V(x_S, \omega) = -g \cdot V_S \tag{41}$$

By superposition

$$V(x_S,\omega) = M_P \cdot Y_{SP} + M_S \cdot Y_{SS} = M_P \cdot Y_{SP} - g \cdot Y_{SS} \cdot V(x_S,\omega) \tag{42}$$

and thus solving for V_S and substituting into Eq.41 gives

$$M_s = M_P \frac{-g \cdot Y_{SP}}{1 + g \cdot Y_{SS}} \tag{43}$$

The vector of structural mode amplitudes $\mathbf{q}(\omega)$ is again the superposition of components $\mathbf{q_P}(\omega)$ due to the primary source M_P and those $\mathbf{q_S}(\omega)$ due to the secondary source M_S, and is given by

$$\mathbf{q}(\omega) = \mathbf{q_p}(\omega) + \mathbf{q_s}(\omega) \cdot \frac{-g \cdot Y_{SP}}{1 + g \cdot Y_{SS}} \tag{44}$$

where $\mathbf{q_P}(\omega)$ and $\mathbf{q_S}(\omega)$ are given by Eq.29 and Eq.31. The cost-function J has a minimum for a particular value of the feedback gain. In fact, if g is equal to zero the system (Figure 30) has a vibrational kinetic energy equal to the uncontrolled case. If the gain g goes to infinity, the secondary actuator behaves like a new "active" boundary condition turning the system into a new one (Figure 31) with different natural frequencies and vibrational kinetic energy (Figure 32).

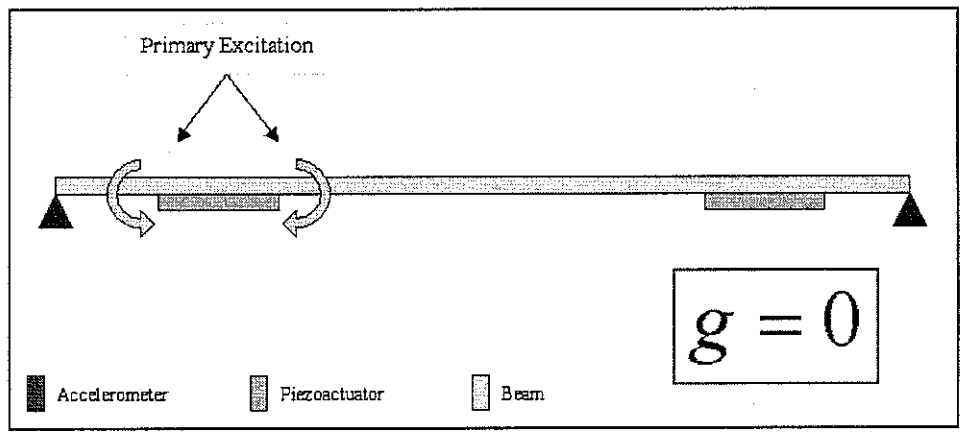

Figure 30 – Equivalent system for g equal to zero

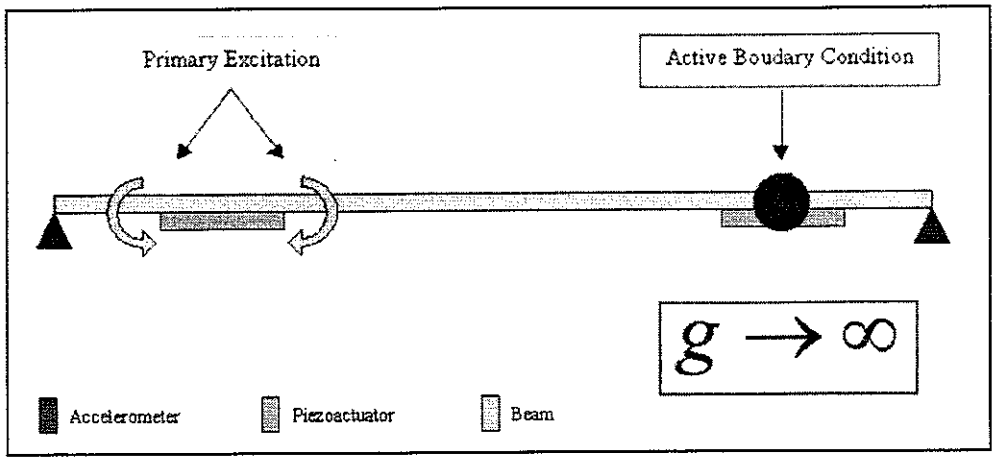

Figure 31 – Equivalent system for g tending to infinity

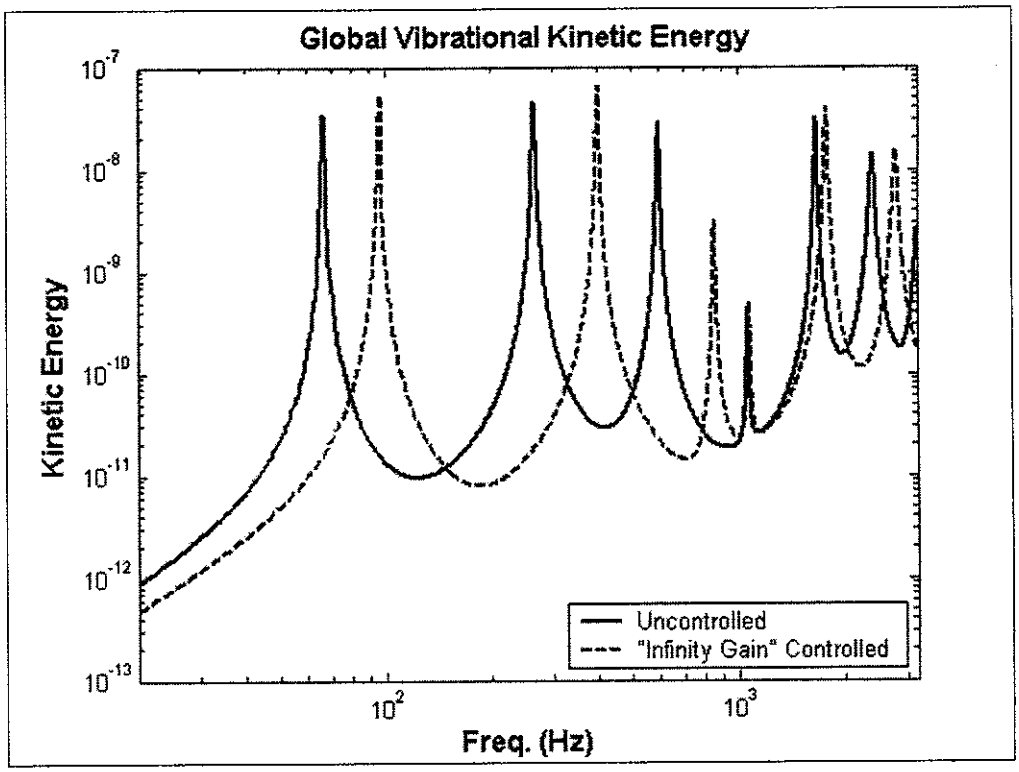

Figure 32 – VKE for g equal to zero and going to infinity (Theory)

The cost-function J is normalized with respect to the uncontrolled case to give

$$J = \frac{\int_{\omega_b} \omega^2 \mathbf{q}^H(\omega) \circ \mathbf{q}(\omega) \cdot d\omega}{\int_{\omega_b} \omega^2 \mathbf{q}_\mathbf{P}^H(\omega) \circ \mathbf{q}_\mathbf{P}(\omega) \cdot d\omega} \tag{45}$$

which is plotted as a function of the feedback gain g in Figure 33.

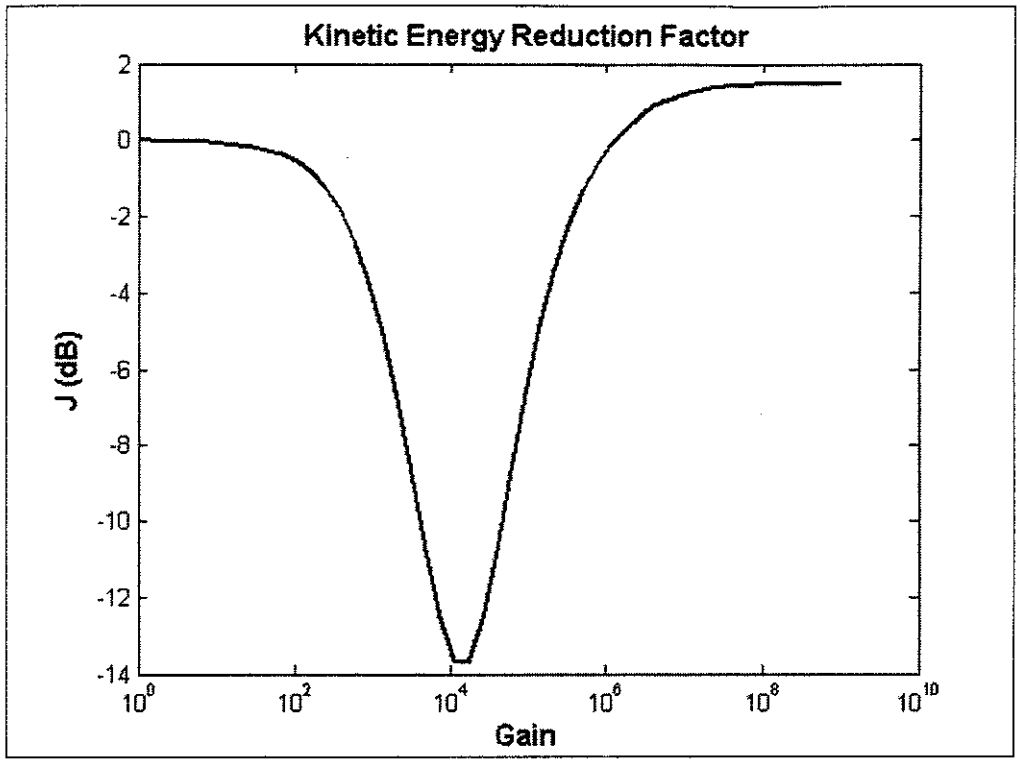

Figure 33 – Kinetic energy reduction factor as a function of the feedback gain (Theoretical Simulation)

7.2 – Theoretical Stability

From Eq.44 it is clear that when the denominator goes to zero, the system response becomes infinite. This is the condition for instability in the feedback control system. The stability equation is

$$1 + g \cdot Y_{SS} = 0 \tag{46}$$

Instability occurs when the feedback gain is increased beyond a certain value, which is referred to as the critical gain. If this is less than the optimum gain for the kinetic energy reduction, then this is a limit for the actual reduction that can be achieved.

The stability of the feedback control system is investigated in this section plotting the Nyquist and Bode plots of the open-loop transfer function Y_{SS}, which is the mobility at the sensor position due to the secondary excitation.

$$Y_{SS} = \frac{V(x_S)}{M_S} = j\omega \cdot \sum_{n=1}^{\infty} \frac{\phi_n(x_S)}{M_n \cdot \left[\omega_n^2 \cdot (1 + j\eta) - \omega^2\right]} \cdot \left[\phi_n'\left(x_S - \frac{d}{2}\right) - \phi_n'\left(x_S + \frac{d}{2}\right)\right] \tag{47}$$

Figure 34 and 35 show the open-loop transfer function Nyquist and Bode plot respectively.

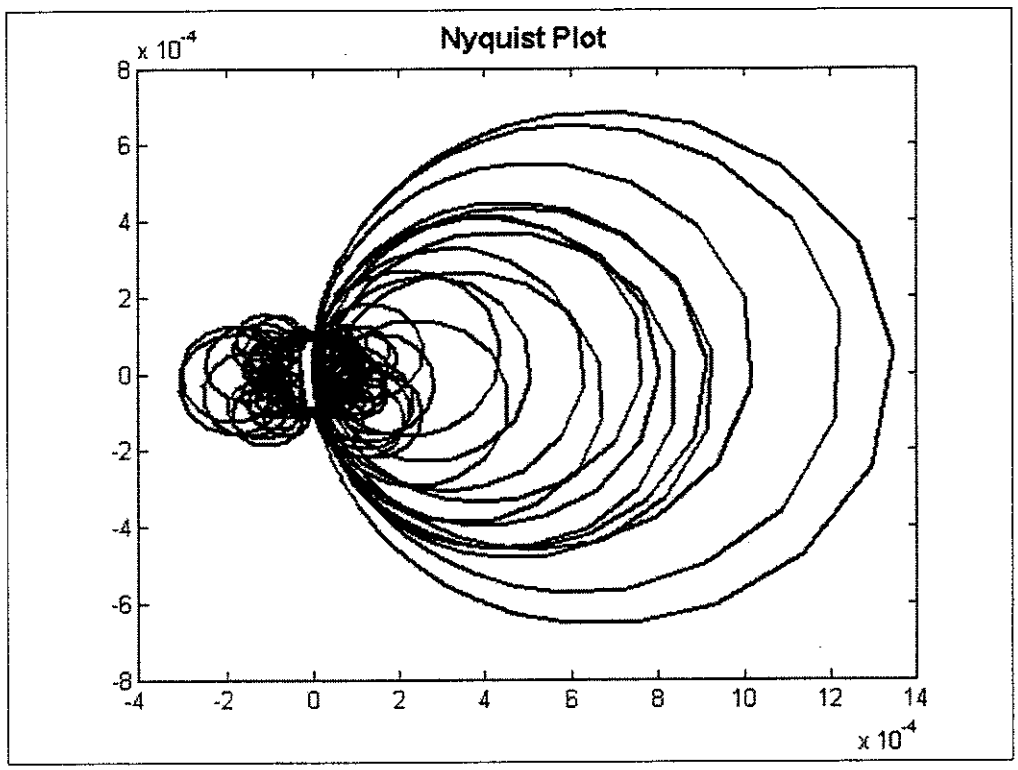

Figure 34 – Open-loop transfer function, Nyquist plot (Theoretical Simulation)

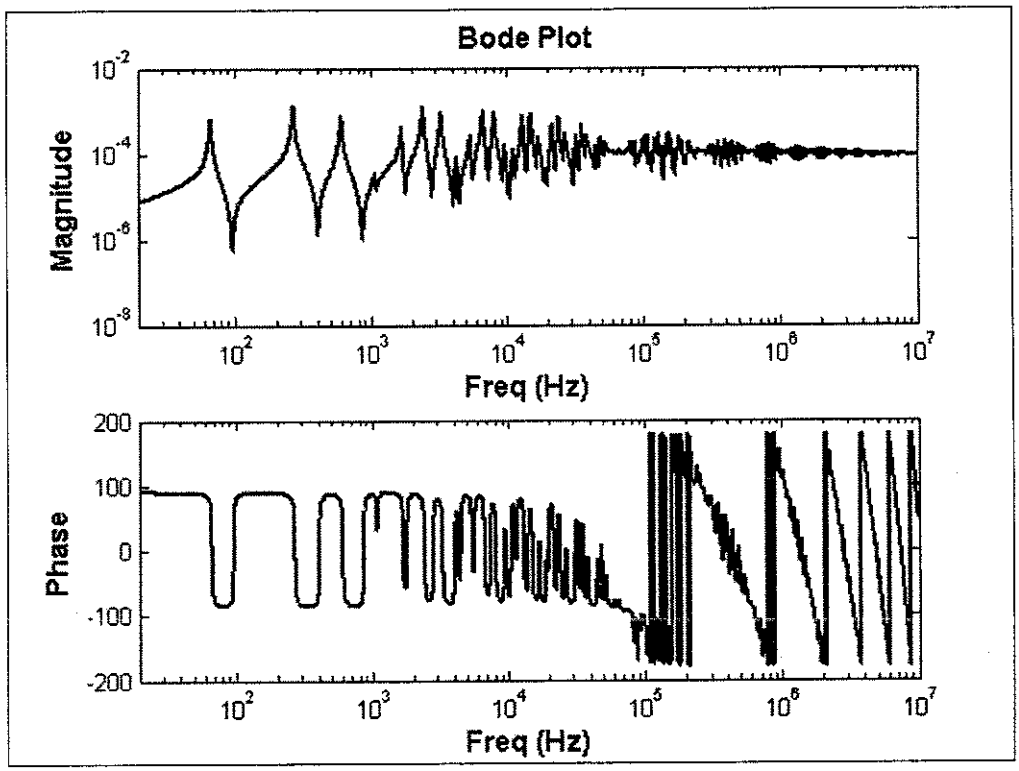

Figure 35 – Open-loop transfer function, Bode plot (Theoretical Simulation)

Theoretical stability has been investigated up to 10^7 Hz, where the magnitude of the Bode plot seems to reach a stable value[1].

From Figure 35 the critical gain is estimated to be around:

$$g_c \cong \frac{1}{3 \cdot 10^{-4}} \approx 3333 \tag{48}$$

The Bode plot illustrates the cause of that instability. In fact, when the frequency is such that the a wavelength is equal to the length of the piezoelectric actuator, the phase of the open-loop transfer function do not recover any more and this is the reason why the loops in the Nyquist plot appear with negative parts real parts causing the system to be only conditionally stable. From Figure 36 the frequency that this occurs is estimated to be around

$$f_c \cong 6.7 \cdot 10^4 \, Hz \tag{49}$$

corresponding to a wavelength of

$$\lambda_c = \frac{2\pi}{\sqrt{2\pi \cdot f_c}} \sqrt[4]{\frac{Y_b \cdot I_b}{\rho_b \cdot A_b}} \cong 0.025m \tag{50}$$

which is an estimate of the piezoelectric actuator length. Figure 33, which represents the kinetic energy reduction factor as a function of the feedback gain, is plotted again in Figure 36 together with the critical gain marked on it. It appears that this is less than the optimum gain and thus the kinetic energy may be only reduced by about 9 dB.

[1] Nevertheless, it should be noted that the Euler-Bernoulli beam model used here, could not be appropriate and might fail sensibly up to these frequencies.

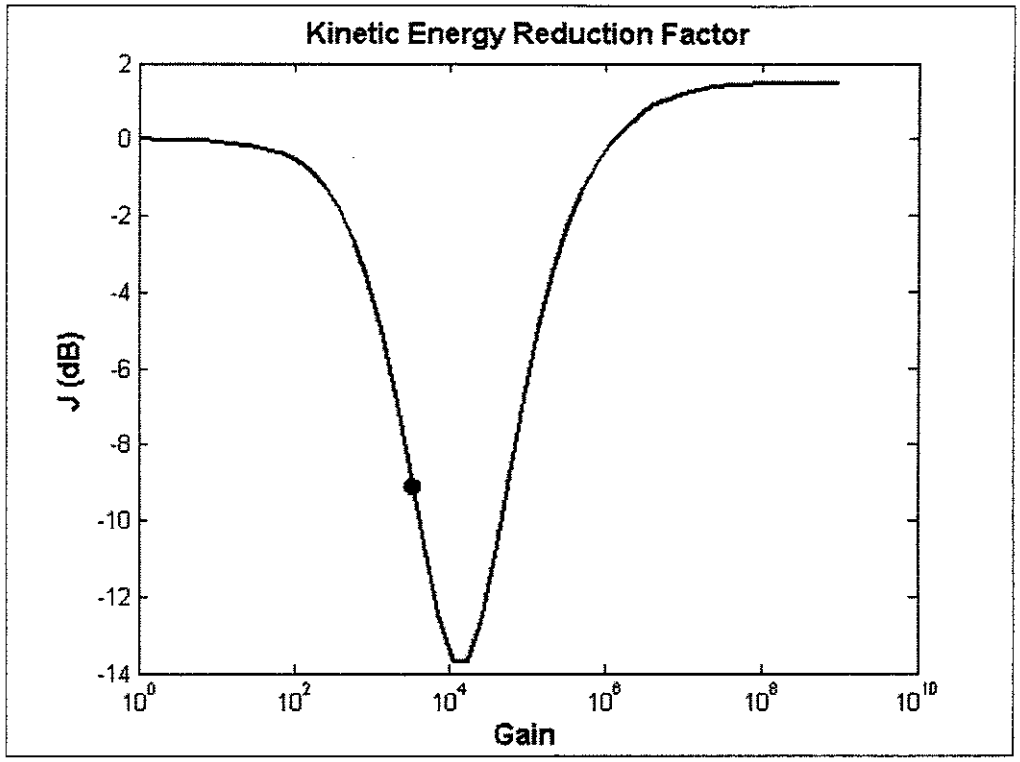

Figure 36 – Kinetic energy reduction factor and critical gain (spot) (Theoretical Simulation)

Figure 37 is a comparison between the uncontrolled and optimal kinetic energy, taking into account the stability requirements. Examining this, it is clear that the effect of the direct velocity feedback is like adding damping to the structure. This is due to the fact that the secondary excitation is proportional to the velocity like a damping force.

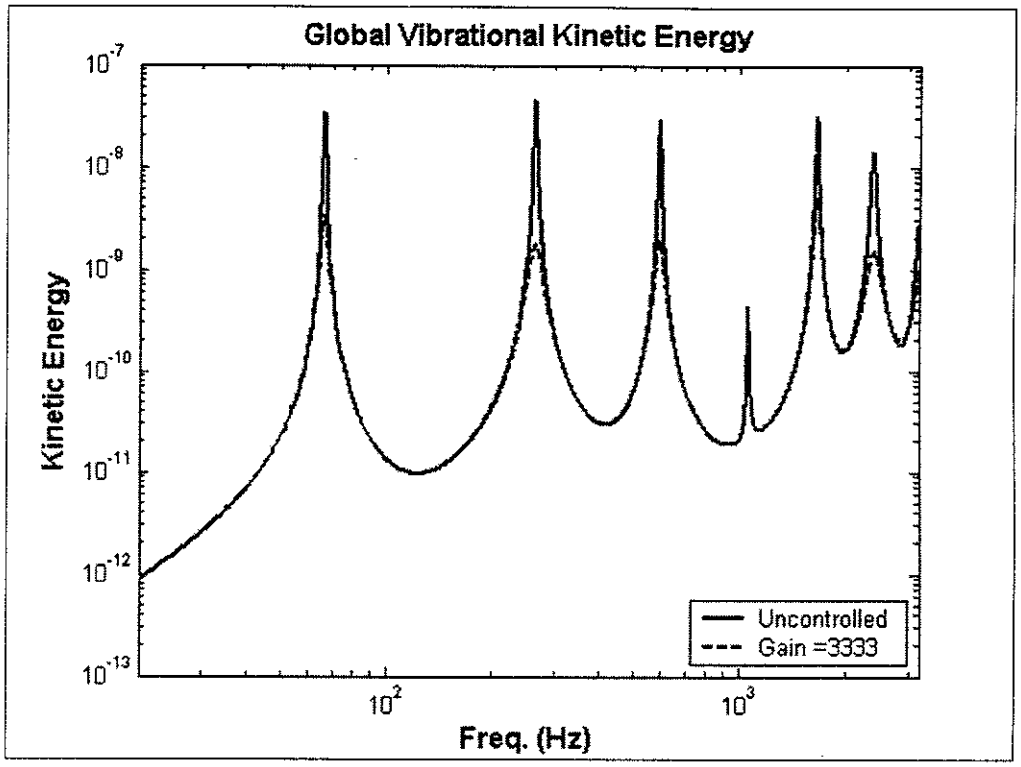

Figure 37 – Uncontrolled and optimized kinetic energy (Theoretical Simulation)

7.3 – Experimental Off-Line Simulation

From an experimental point of view, the global vibrational kinetic energy of the beam is estimated from Eq. 23, where the velocity at each point along the beam is given as the superposition of the velocity at that point due to the primary and secondary excitation, as:

$$V(x_e,\omega) = M_p Y_p(x_e,\omega) + M_s Y_s(x_e,\omega) \tag{51}$$

With reference to Figures 38 and 39, Eq.41 can be rewritten as:

$$M_s = -A_S \cdot g_a \cdot H_a \cdot g \cdot H_i \cdot c_p \tag{52}$$

where A_S is the acceleration of the beam at the sensor position, g_a is the signal conditioning gain, H_a is the accelerometer transfer function, g is the feedback gain, H_i is the integrator transfer function and c_p is the piezoelectric actuator transfer function.

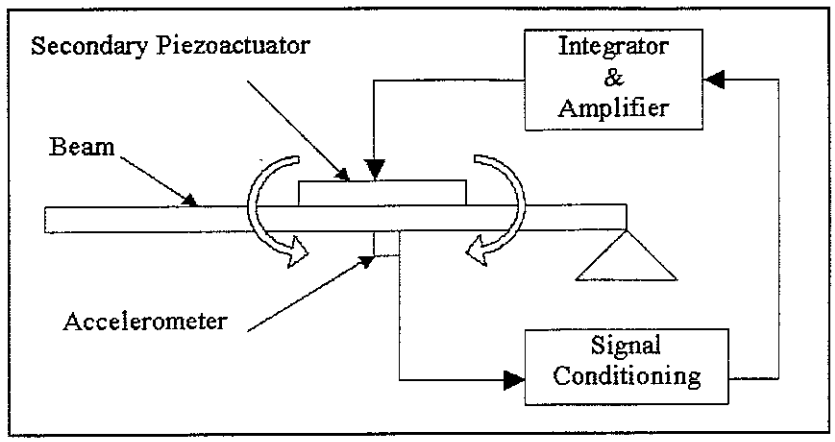

Figure 38 – Actual Feedback Loop

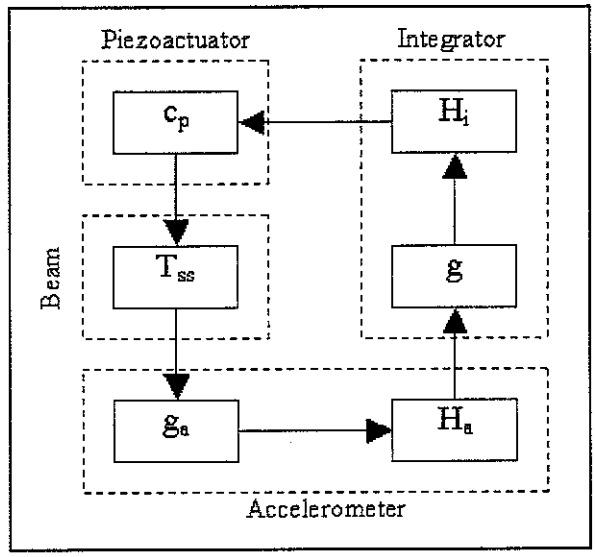

Figure 39 – Actual Feedback Loop Block Diagram

The acceleration at the sensor position A_S, may by written using the superposition principle as

$$A_S = M_P T_{SP} + M_S T_{SS} \tag{53}$$

Combining Eq.52 and Eq.53, Eq.51 can be written as

$$V(x_e,\omega) = M_p\left[Y_p(x_e,\omega) - Y_s(x_e,\omega)\frac{g_a \cdot H_a \cdot g \cdot H_i \cdot c_p \cdot T_{SP}}{1 + g_a \cdot H_a \cdot g \cdot H_i \cdot c_p \cdot T_{SS}}\right] \tag{54}$$

Substituting Eq.54 into Eq.23, one gets the kinetic energy as a function of the feedback gain g and all the real transfer functions present in the feedback loop.

For the evaluation of the cost-function J, the following equation is used rather than Eq.45

$$J = \frac{\sum_i \left(\sum_{e=1}^{p} m_e \cdot Y(x_e, \omega_i) \cdot Y^*(x_e, \omega_i) \right)}{\sum_i \left(\sum_{e=1}^{p} m_e \cdot Y_P(x_e, \omega_i) \cdot Y_P^*(x_e, \omega_i) \right)} \tag{55}$$

Figure 40 shows the cost-function J, i.e., the kinetic energy reduction factor, as a function of the feedback gain, for the theoretical and off-line simulation.

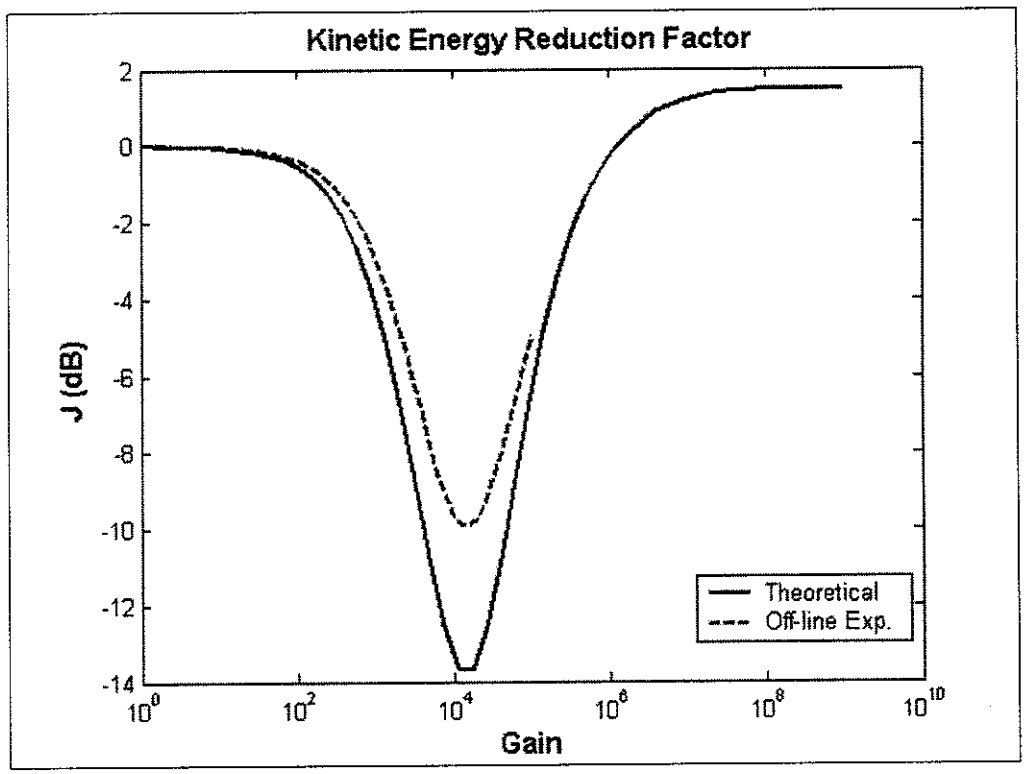

Figure 40 – Kinetic energy reduction factor (Theoretical and Off-line Simulation)

7.4 – Experimental Stability

Eq.46, which determines the stability of the feedback system in the ideal case, is now substituted by the denominator of Eq.54, that is:

$$1 + g_a \cdot H_a \cdot g \cdot H_i \cdot c_p \cdot T_{SS} = 0 \tag{56}$$

Figure 41 is the Bode plot of the accelerance as measured by the accelerometer (PCB model 352C22) out from the signal conditioning (PCB model 442C04), i.e. $T_{SS} \cdot g_a \cdot H_a$, compared to the theoretical plot.

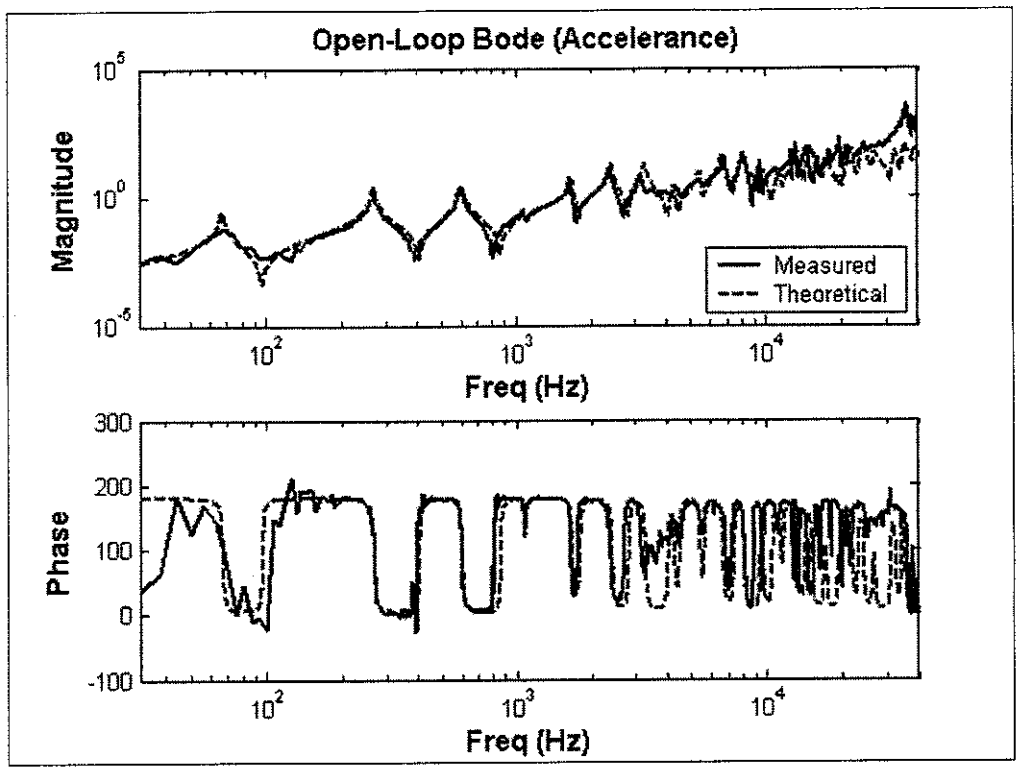

Figure 41 – Theoretical and measured accelerance

Figure 42 is the Bode plot of the ideal and measured integrator frequency response function.

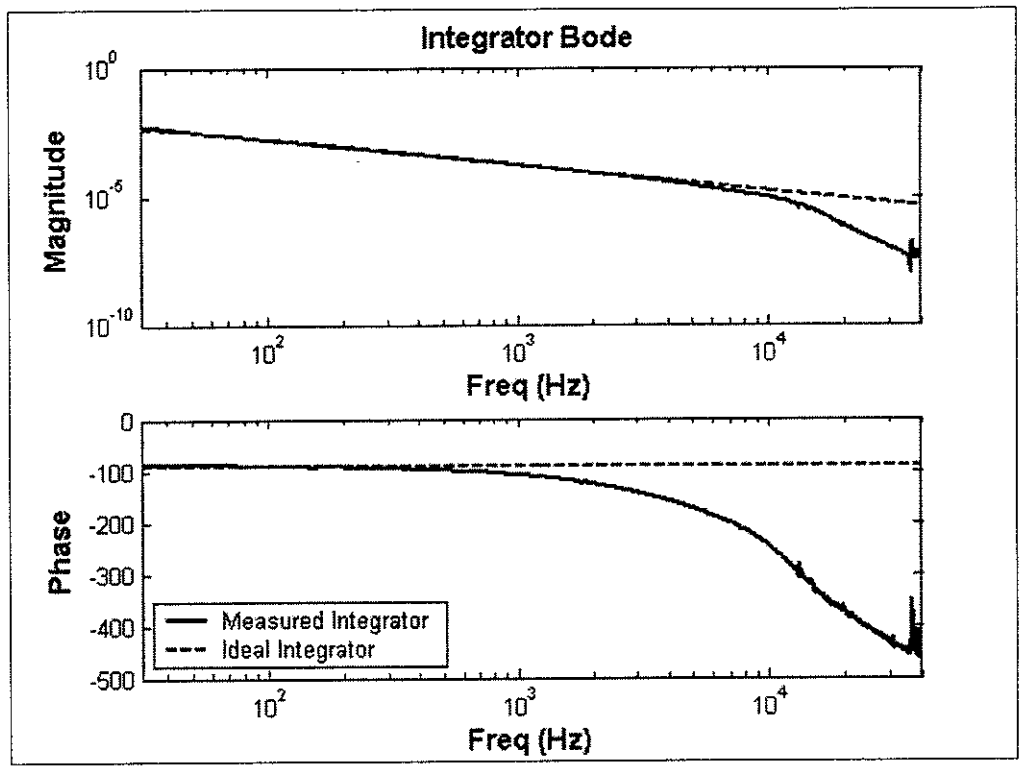

Figure 42 – Theoretical and measured integrator FRF

The stability of the close-loop system is investigated again using the Nyquist and Bode plot of the open-loop transfer function, which are shown in Figure 43 and 44 respectively.

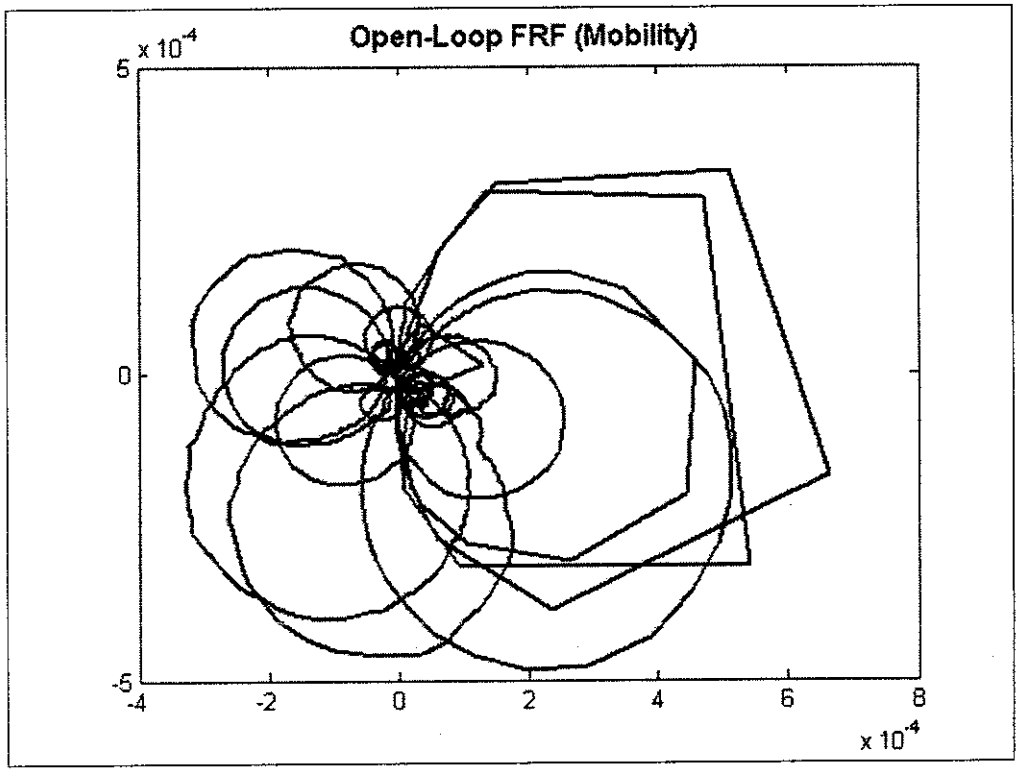

Figure 43 – Open-loop transfer function, Nyquist plot (Measurement)

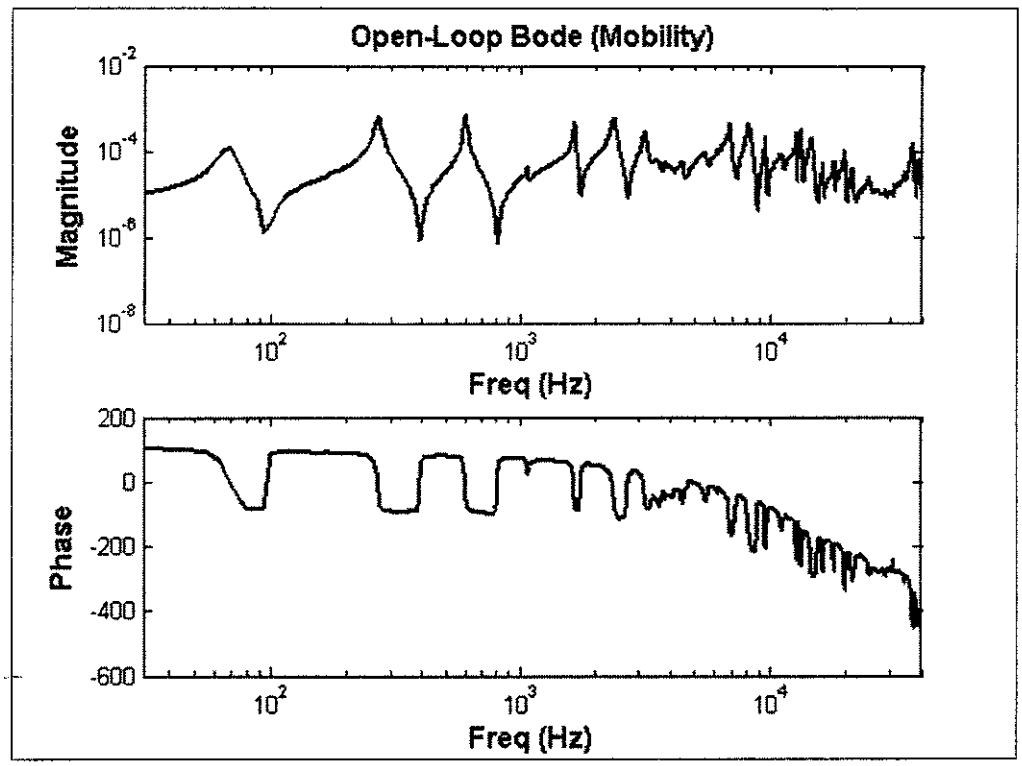

Figure 44 – Open-loop transfer function, Bode plot (Measurement)

From the Nyquist plot in Figure 44 the critical gain is now estimated to be around:

$$g_c \cong \frac{1}{3.5 \cdot 10^{-4}} \approx 2860 \tag{57}$$

which is a little bit lower than the theoretical one. Figure 45 shows the kinetic energy reduction factor from the off-line simulation together with the critical gain marked on it.

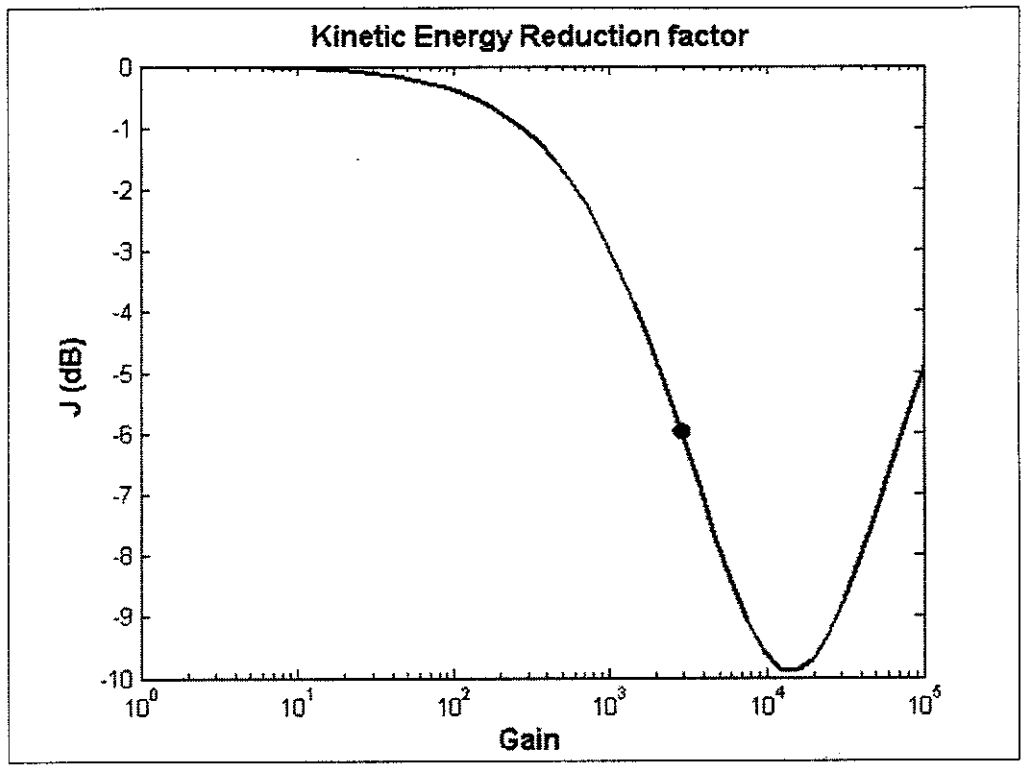

Figure 45 – Kinetic energy reduction factor and critical gain (spot) (Off-Line Simulation)

One may notice that now the instability is not due to the same reason as described in Section 7.b, but it is due to the combination of all the actual instrument transfer functions, which causes the phase angle in the Bode plot not to recover and in the Nyquist plot shifts the loops onto the negative side of the real axis, encircling the Nyquist point when increasing the feedback gain.

7.5 – Experimental Results

An experiment was conducted to validate the predictions from simulations. The experimental setup is shown in Figure 46.

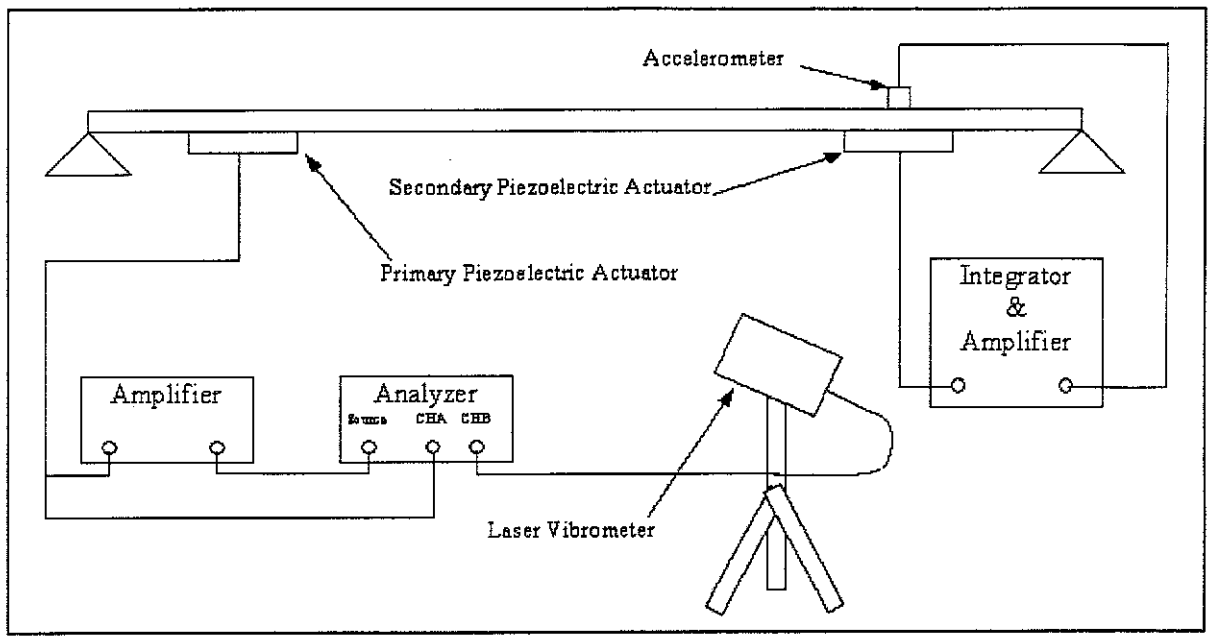

Figure 46 – Experimental setup of the feedback control system

The feedback gain is increased from zero (uncontrolled system) to the physical limit of the amplifier. The vibrational kinetic energy of the beam is thus estimated, for each value of the feedback gain, using Eq.23. The kinetic energy reduction factor is then evaluated by Eq.55 and shown in Figure 47 together with the one from the off-line simulation.

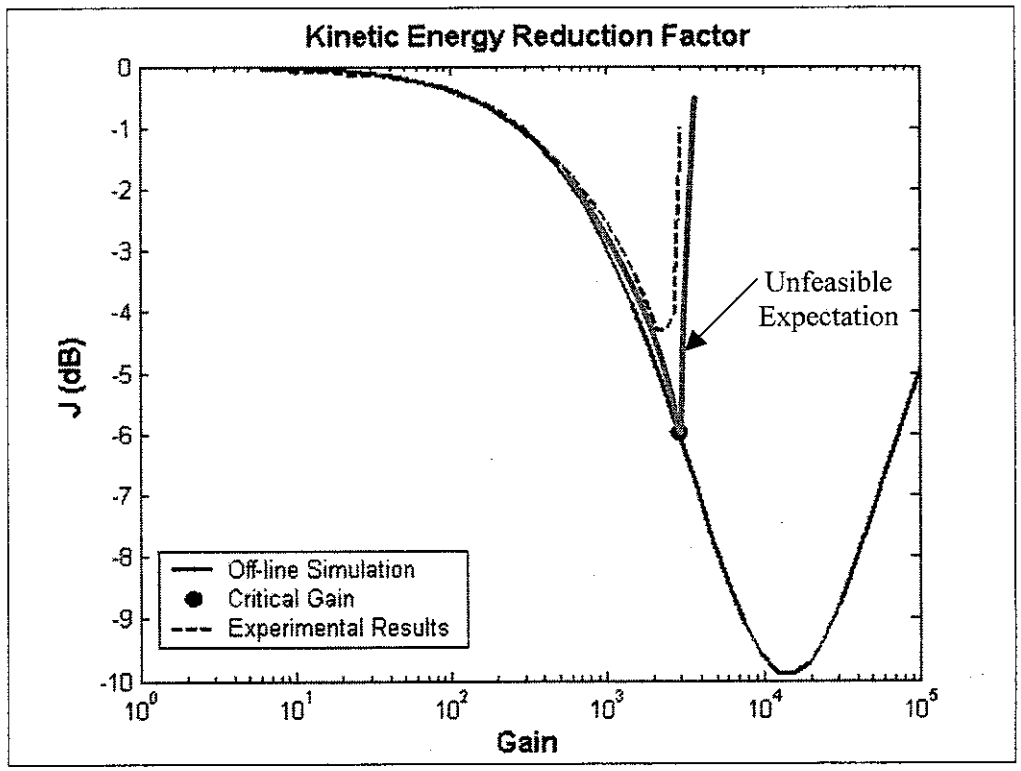

Figure 47 – Kinetic energy reduction factor and critical gain (Off-line Simulation and Measurement)

As may be noticed from Figure 47, the gain of the experimental results where the kinetic energy reduction factor reaches a minimum, corresponds to the critical gain as evaluated from off-line simulation. This is consistent with the fact that increasing the gain beyond the critical value, the instability in the system will cause the vibrational kinetic energy to increase. The experimental results also show that the kinetic energy may only be reduced by about 4dB, and thus the actual reduction is lower than the predicted. This is due to the fact that off-line simulation does not take into consideration the effects caused by instability in the neighbourhood of the critical gain. An unfeasible expectation is also plotted in Figure 47.

7.6 –Improving Theoretical Stability

From section 7.2 it is clear that the critical gain, which comes from the theoretical analysis, is a limit that can not be exceeded. It is of interest to see if there is a way to keep this limit as high as possible. The stability limit comes from the presence of the loops of the open-loop transfer function on the left hand side of the Nyquist plot of Figure 34. A way to increase the value of the critical gain could be to keep those loops as closer to the imaginary axis as possible. This could be achieved by adding an additional roll-off in the frequency response function plotted in Figure 35. A lumped mass concentrated at the sensor position be helpful in this respect, since the mobility of a mass reduces with frequency. Figure 48 illustrates the addition of the lumped mass.

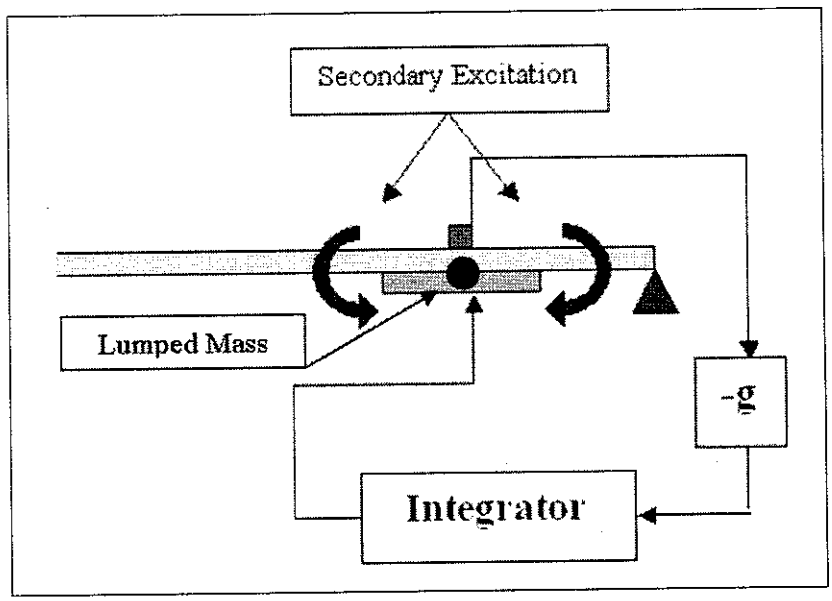

Figure 48 – Sketch of the Direct Velocity Feedback Control System with added Lumped Mass

To write an expression of the mass-modified open-loop transfer function, the mobility method is used.

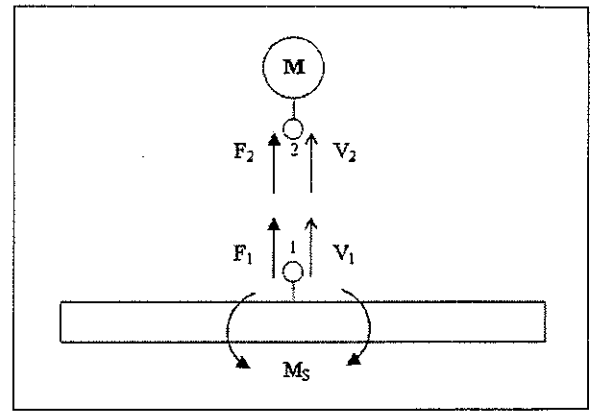

Figure 49 – Sketch of the Lumped Mass addition to the open-loop transfer function

Point 1 and point 2 in Figure 49 are rigidly connected and both coincide with the sensor position and so the following equations hold

$$V_1 = V_2 = V_S \tag{58.a}$$
$$F_1 + F_2 = 0 \tag{58.b}$$
$$V_2 = F_2 \cdot Y_{22} \tag{58.c}$$
$$V_1 = F_1 \cdot Y_{11} + M_S \cdot Y_{1S} \tag{58.d}$$

Where Y_{22} is the mobility of the mass M, Y_{11} is the point mobility at the sensor position due to a unitary force and Y_{1S} is the mobility at the sensor position due to a unitary moment and is given by Eq. 47. The expressions for these mobilities are given by

$$Y_{22} = Y_{S2} = \frac{1}{j\omega \cdot M} \tag{59.a}$$
$$Y_{11} = Y_{S1} = j\omega \cdot \sum_{n=1}^{\infty} \frac{\phi_n(x_S)}{M_n \cdot \left[\omega_n^2 \cdot (1 + j\eta) - \omega^2\right]} \left[\phi_n(x_S)\right] \tag{59.b}$$
$$Y_{1S} = Y_{SS} = j\omega \cdot \sum_{n=1}^{\infty} \frac{\phi_n(x_S)}{M_n \cdot \left[\omega_n^2 \cdot (1 + j\eta) - \omega^2\right]} \left[\phi_n'\left(x_S - \frac{d}{2}\right) - \phi_n'\left(x_S + \frac{d}{2}\right)\right] \tag{59.c}$$

Combining Eq. 58.a-d the ratio V_S/M_S is given by

$$\frac{V_S}{M_S} = Y_{SS} \cdot \frac{Y_{S2}}{Y_{S2} + Y_{S1}} \tag{60}$$

Eq.60 represents the lumped-mass modified open-loop transfer function.

Increasing the value of the mass M results in a roll-off which improves the stability of the system. The greater the mass, the greater the critical feedback gain that can be achieved.

Figure 50 and 51 show the Bode and Nyquist plot respectively of the open-loop transfer function with a lumped mass equal to 1% of the beam mass. Figure 52 and 53 show the Bode and Nyquist plot respectively of the open-loop transfer function with a lumped mass equal to 15% of the beam mass.

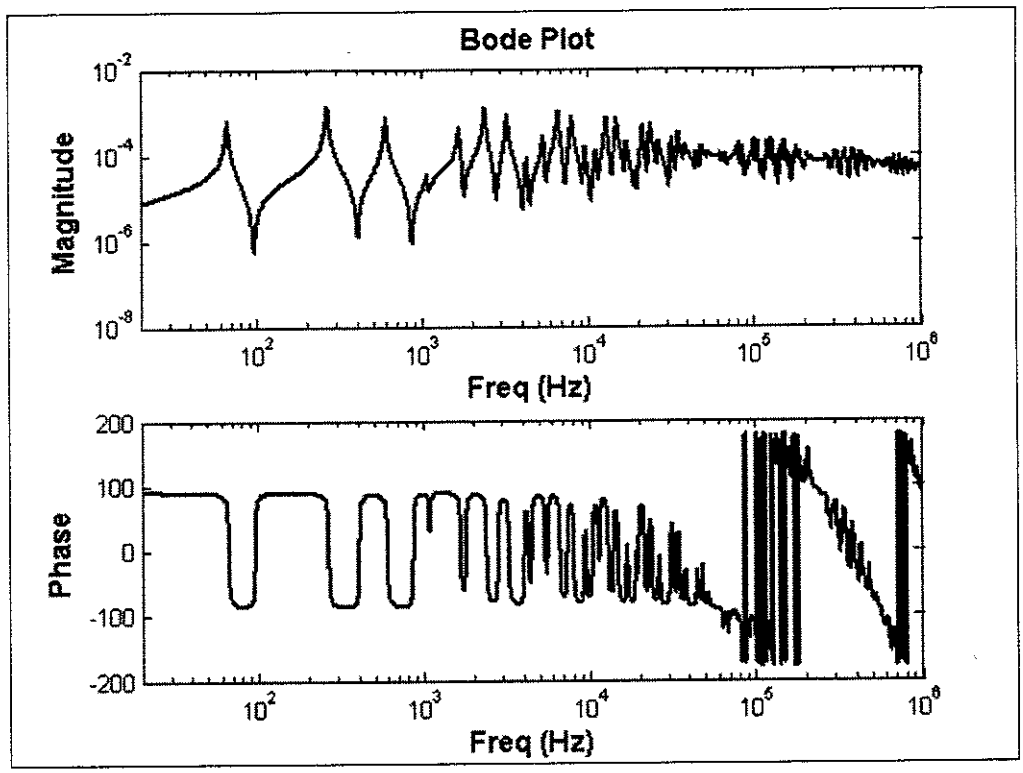

Figure 50 – Open-loop transfer function, Bode plot, for M=1% of the Beam Mass (Theoretical Simulation)

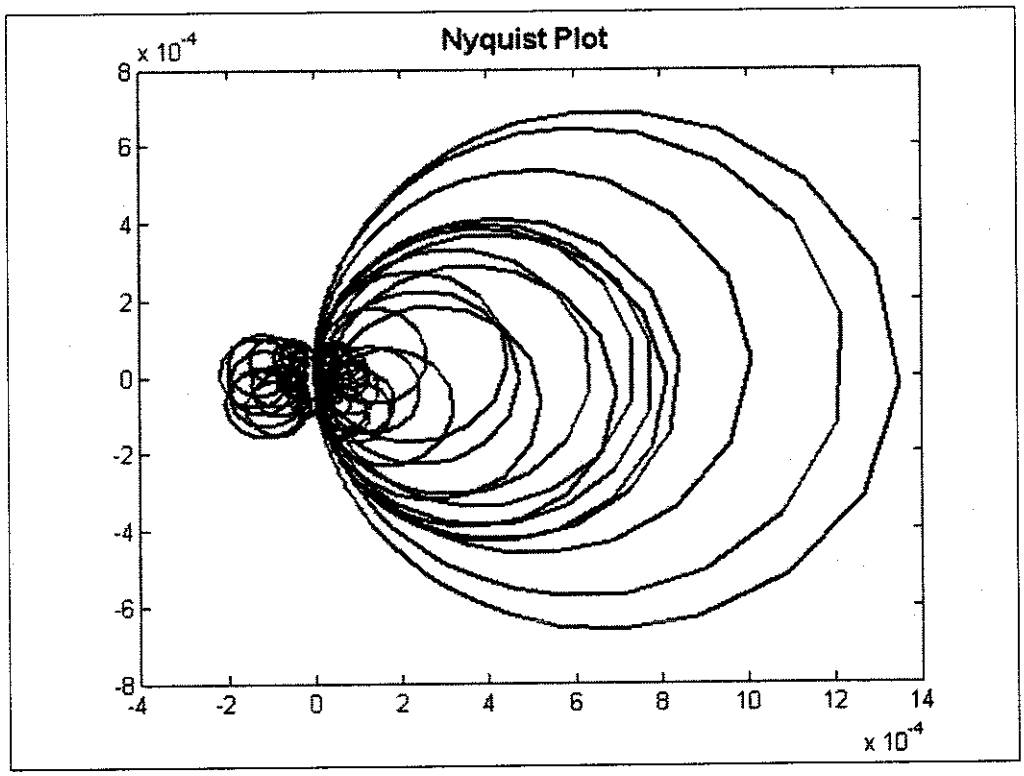

Figure 51 – Open-loop transfer function, Nyquist plot, for M=1% of the Beam Mass (Theoretical Simulation)

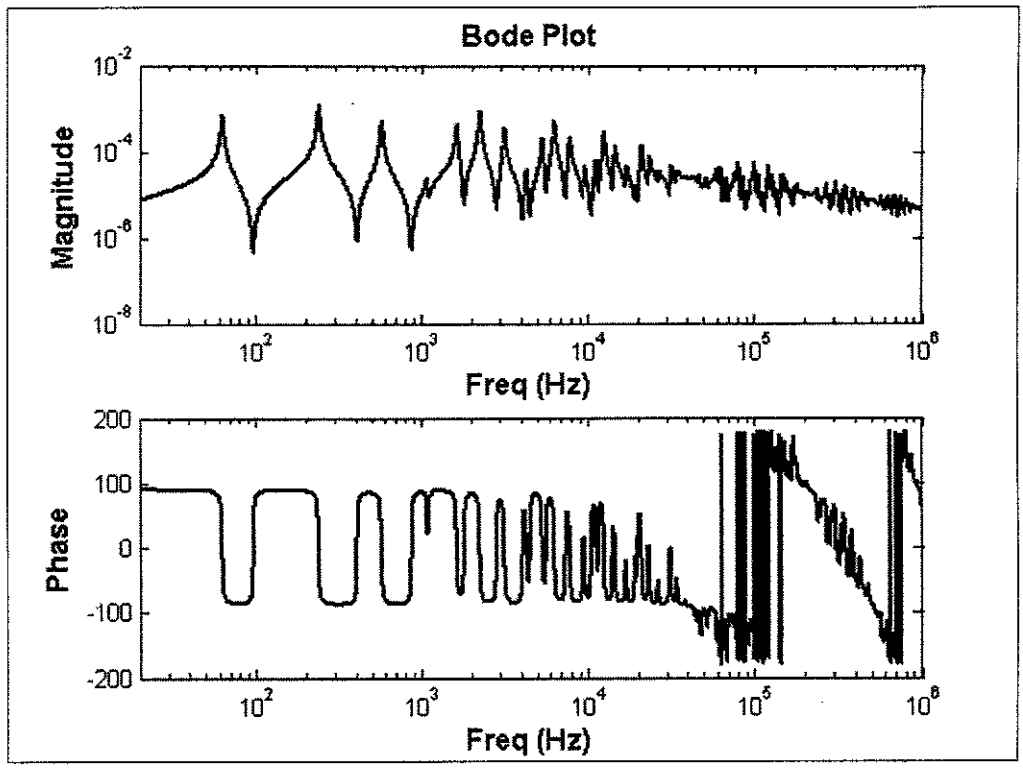

Figure 52 – Open-loop transfer function, Bode plot, for M=15% of the Beam Mass (Theoretical Simulation)

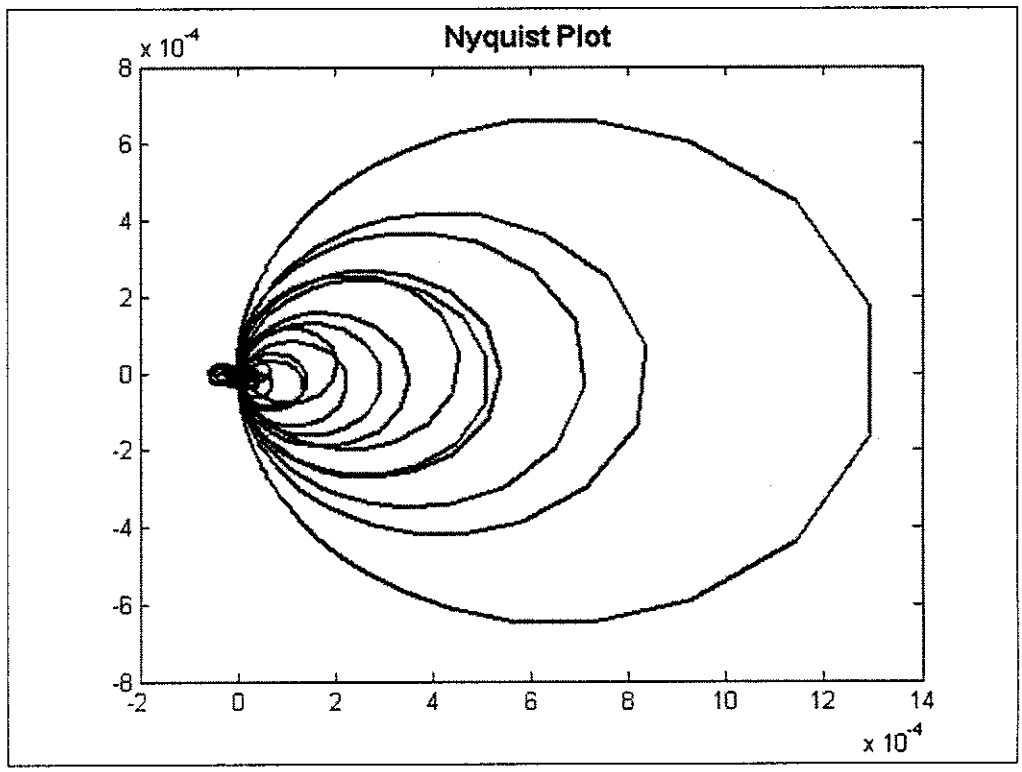

Figure 53 – Open-loop transfer function, Nyquist plot, for M=15% of the Beam Mass (Theoretical Simulation)

Since the mechanical system is now changed by the addition of the lumped mass M, its global vibrational kinetic energy will also be changed. The approach followed here is the one of section 7.3, where the global vibrational kinetic energy of the beam is estimated from Eq. 23 which is repeated here for convenience

$$VKE(\omega) \cong \frac{1}{2}\sum_{e=1}^{p} m_e \cdot V(x_e,\omega)\cdot V^*(x_e,\omega) = \frac{1}{2}M^2\sum_{e=1}^{p} m_e \cdot Y(x_e,\omega)\cdot Y^*(x_e,\omega) \tag{23}$$

The beam is now split in 23 elements so that the centre of the 18-th coincides with the location of the lumped mass; the mass of this element is hence updated with the addition of the mass M.
The velocity at each point along the beam is now given as the superposition of the velocity at that point due to the primary excitation M_P, the secondary excitation M_S and the force F_1 due to the lumped mass M, as:

$$V(x_e,\omega) = M_p Y_p(x_e,\omega) + M_s Y_s(x_e,\omega) + F_1 Y_1(x_e,\omega) \tag{61}$$

Figure 54 is a sketch of the whole system modified by the addition of the lumped mass.

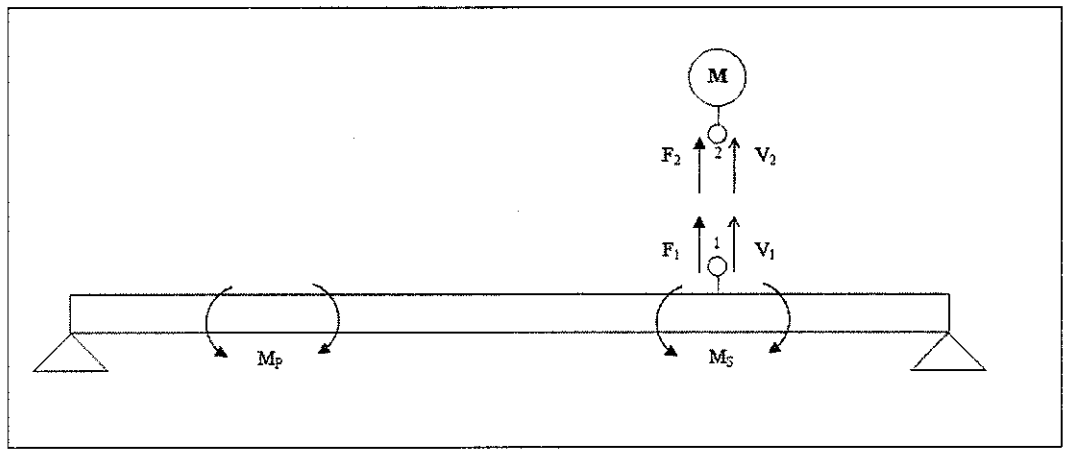

Figure 54 – Sketch of the Lumped Mass addition to the whole system

The following equations now hold:

$$V_1 = V_2 = V_S \tag{62.a}$$
$$F_1 + F_2 = 0 \tag{62.b}$$
$$V_2 = F_2 \cdot Y_{22} \tag{62.c}$$
$$V_1 = F_1 \cdot Y_{11} + M_S \cdot Y_{1S} + M_P \cdot Y_{1P} \tag{62.d}$$

Solving Eq. 62.a-d for V_S gives

$$V_S = \left(M_P Y_{SP} + M_S Y_{SS}\right) \cdot \frac{Y_{S2}}{Y_{S2} + Y_{S1}} \tag{63}$$

Combining Eq. 63 and Eq. 41, gives a new expression for the secondary moment as a function of the primary moment and the feedback gain, as given below:

$$M_s = M_P \frac{-g \cdot Y_{SP} \cdot \dfrac{Y_{S2}}{Y_{S2} + Y_{S1}}}{1 + g \cdot Y_{SS} \cdot \dfrac{Y_{S2}}{Y_{S2} + Y_{S1}}} \tag{64}$$

Eq. 64 is now used instead of Eq. 43, and the stability equation is given by

$$1 + g \cdot Y_{SS} \cdot \frac{Y_{S2}}{Y_{S2} + Y_{S1}} = 0 \tag{65}$$

The expression of the force F_1 is determined by combining Eq. 62.a-c and Eq. 63 as to give:

$$F_1 = -\frac{\left(M_P Y_{SP} + M_S Y_{SS}\right)}{Y_{S2} + Y_{S1}} \tag{66}$$

Considering Eq. 64 and Eq. 66, Eq. 61 is rewritten as:

$$V_e = M_p \cdot \left[\left(Y_{eP} - Y_{e1} \cdot \frac{Y_{SP}}{Y_{S2} + Y_{S1}} \right) + \left(Y_{eS} - Y_{e1} \cdot \frac{Y_{SS}}{Y_{S2} + Y_{S1}} \right) \cdot \frac{-g \cdot Y_{SP} \cdot \dfrac{Y_{S2}}{Y_{S2} + Y_{S1}}}{1 + g \cdot Y_{SS} \cdot \dfrac{Y_{S2}}{Y_{S2} + Y_{S1}}} \right] \tag{67}$$

Thus the global vibrational kinetic energy is estimated by Eq. 23 and the cost-function J is evaluated by Eq.68, which is used instead of Eq. 55.

$$J = \frac{\sum_i \left(\sum_{e=1}^{p} m_e \cdot Y(x_e, \omega_i) \cdot Y^*(x_e, \omega_i) \right)}{\sum_i \left(\sum_{e=1}^{p} m_e \cdot \tilde{Y}_P(x_e, \omega_i) \cdot \tilde{Y}_P{}^*(x_e, \omega_i) \right)} \tag{68}$$

where now:

$$Y(x_e, \omega_i) = \frac{V_e}{M_p} = \left[\left(Y_{eP} - Y_{e1} \cdot \frac{Y_{SP}}{Y_{S2} + Y_{S1}} \right) + \left(Y_{eS} - Y_{e1} \cdot \frac{Y_{SS}}{Y_{S2} + Y_{S1}} \right) \cdot \frac{-g \cdot Y_{SP} \cdot \dfrac{Y_{S2}}{Y_{S2} + Y_{S1}}}{1 + g \cdot Y_{SS} \cdot \dfrac{Y_{S2}}{Y_{S2} + Y_{S1}}} \right] \tag{69.a}$$

$$\tilde{Y}_P(x_e, \omega_i) = \left. \frac{V_e}{M_p} \right|_{g=0} = \left[\left(Y_{eP} - Y_{e1} \cdot \frac{Y_{SP}}{Y_{S2} + Y_{S1}} \right) \right] \tag{69.b}$$

Eq. 68 is thus plotted in Figure 55 as a function of the feedback gain g, for different values of the mass M.

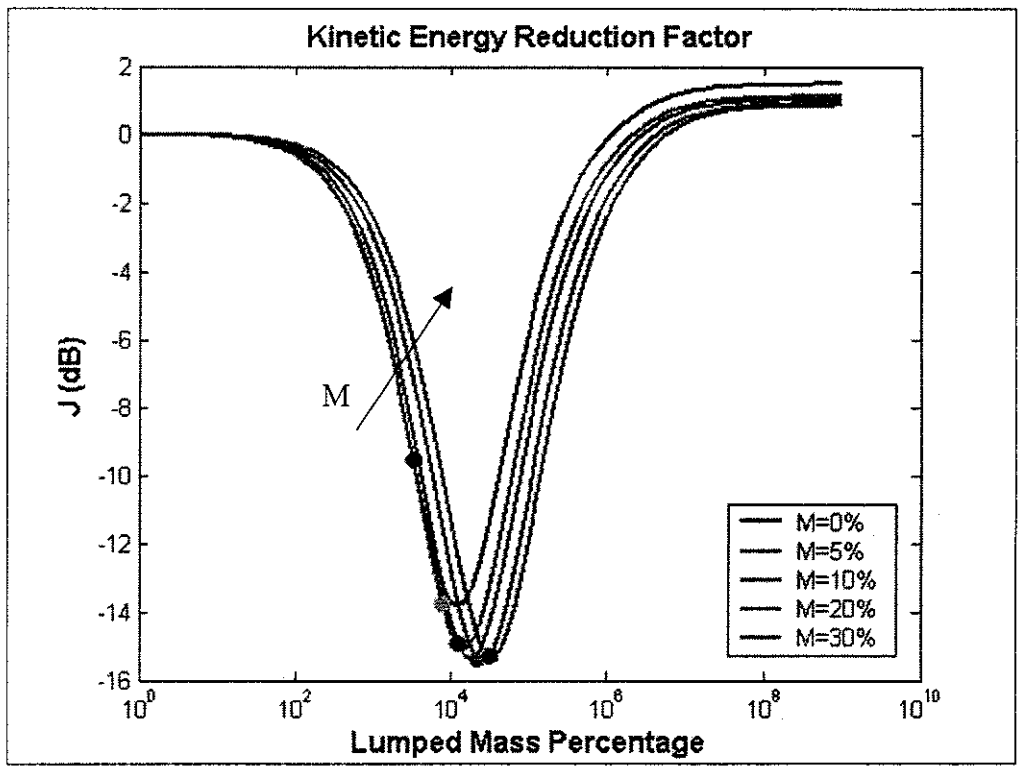

Figure 55 – Kinetic energy reduction factor as a function the feedback gain for different values of M

As can be seen from Figure 55, increasing the mass M from 0% to roughly 20% of the beam mass results in increasing the maximum kinetic energy reduction. Beyond that value, the maximum

kinetic energy reduction starts decreasing again, but with a lower rate. Both the optimum and critical feedback gain increase when increasing the mass M, though with different rates. For each value of M, the optimum feedback gain and the corresponding kinetic energy reduction factor are evaluated from Figure 55; the critical feedback gain and its correspondent kinetic energy reduction factor are estimated from stability requirements using the Nyquist diagram. Figure 56 shows the optimal and critical kinetic energy reduction factor J as a function of M.

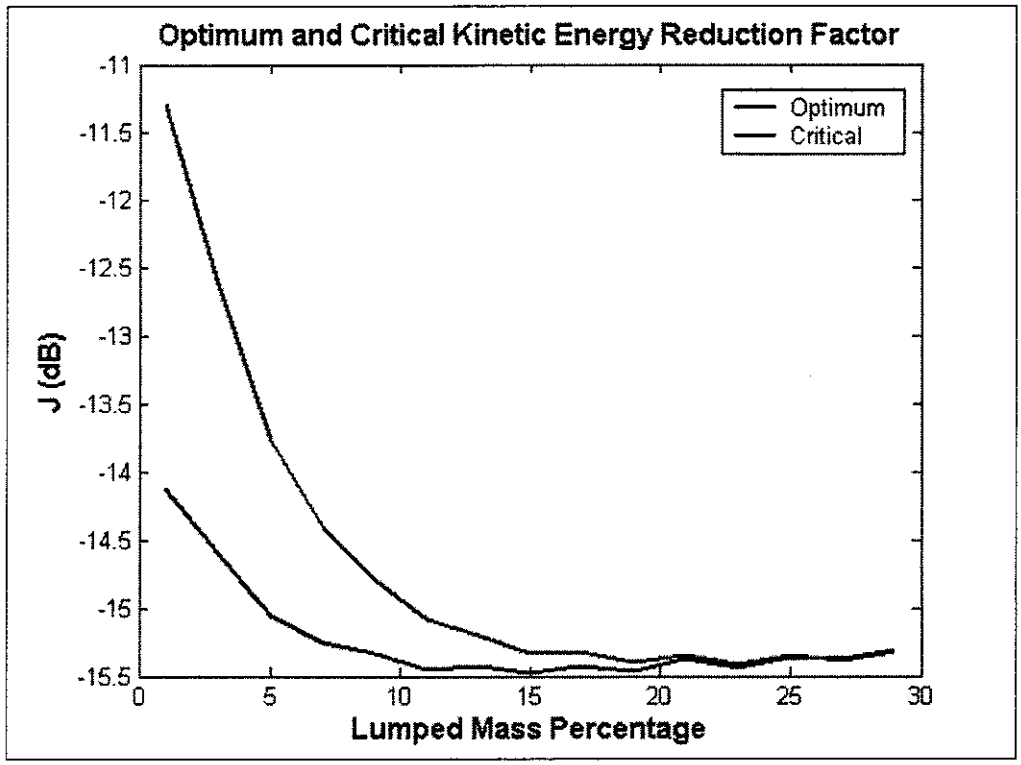

Figure 56 – Optimum and Critical Kinetic energy reduction factor as a function of M

From Figure 56 it can be seen that the performance of the system can be improved by simply adding a concentrated mass at the sensor position. The optimal value of the lumped mass to be added will thus result from a trade-off between the kinetic energy reduction that may be achieved and the amount of mass that has to be added to the system. For instance, if the lumped mass is equal to 10% of the beam mass, the global vibrational kinetic energy can be reduced by about 15 dB. Figure 57 shows a comparison between the cost-function J as a function of the feedback gain for M equal to 10% of the beam mass and the same quantity without the addition of the mass M, as already obtained in section 7.2. In the same figure are also shown the critical gains for the two cases. Figure 58 is a comparison between the uncontrolled and optimal kinetic energy with the addition of a 10% lumped mass.

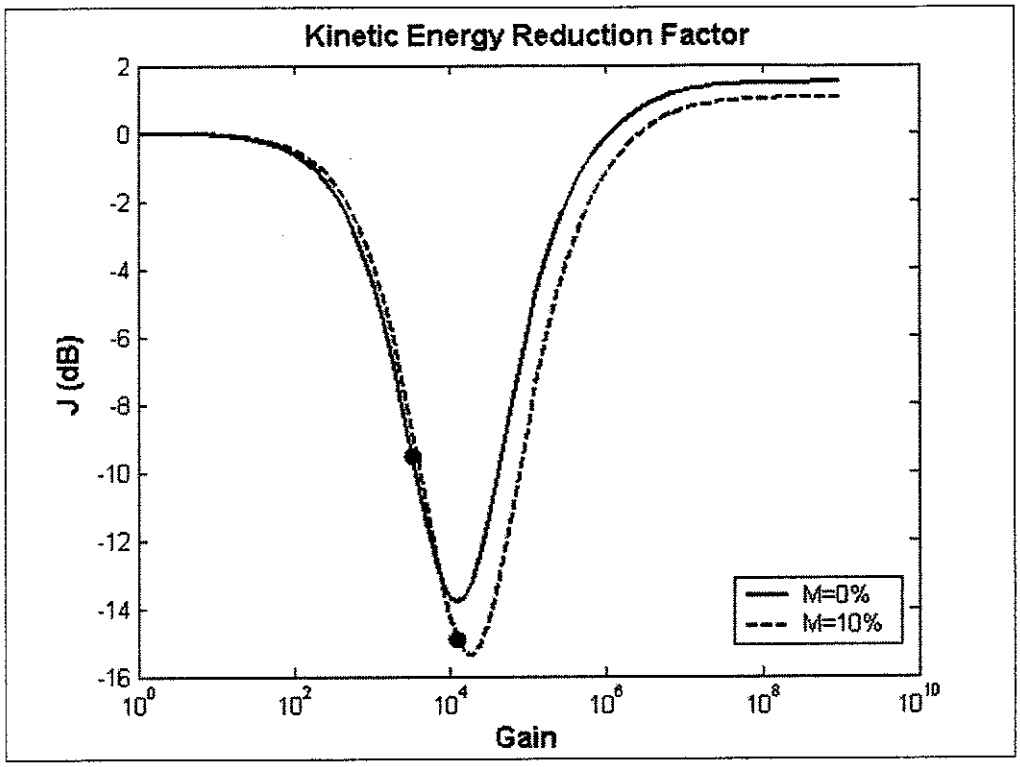

Figure 57 – Kinetic energy reduction factor as a function of the feedback gain for M=0% and M=10%

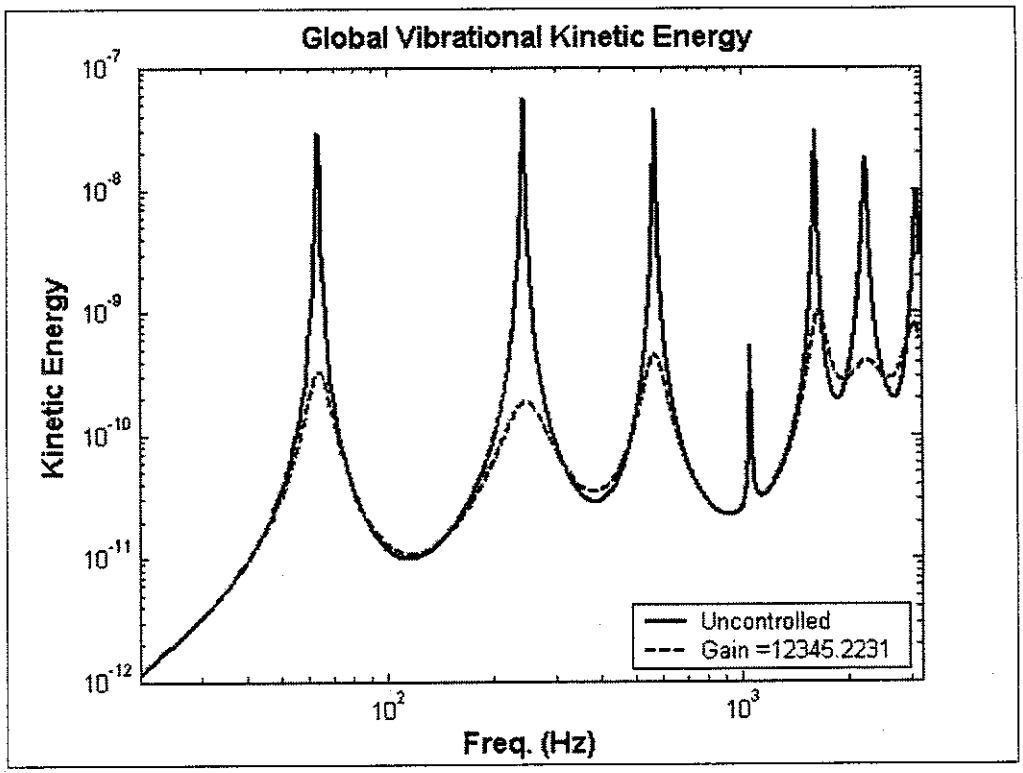

Figure 58 – Uncontrolled and optimized kinetic energy with 10% Lumped Mass (Theoretical Simulation)

8 – Conclusions

Active vibration control of a beam using distributed piezoelectric actuators has been investigated. Feedforward and Direct Velocity Feedback control systems have been studied. Performances of the systems have been presented in terms of global vibrational kinetic energy reduction of the beam in a given bandwidth. A feedforward strategy is effective when the structure to be controlled is excited by a primary excitation at a single frequency. In fact in order to provide active damping to the beam for a wide frequency range, the controller realization turns out to be difficult. Theoretical predictions have been compared with experimental off-line simulation, showing very good agreement. When active damping is needed in a wider frequency band, Direct Velocity Feedback may be used and it provides effective damping in spite of having a very simple controller. However, when the actuator and the sensor are non-collocated (as in the case of velocity sensor/moment pair), there is a limitation on the feedback gain due to stability requirements. The theoretical instability was verified to be due to the actual sensor/actuator non-collocation. From an experimental point of view, the instability is due to the fact that all the system components have non-ideal transfer functions, which are different from the theoretical ones. It is the combination of those transfer functions that can make the system unstable. Experimental results also showed that the kinetic energy reduction factor reaches a minimum at the critical gain predicted from the off-line simulation. The effects of the instability in the neighbourhood of the critical gain may be estimated by experimental off-line simulation. The theoretical stability limit may be improved by adding a lumped mass at the sensor location.

References

[1] C. M. Harris, *Shock and Vibration Handbook*, 4th Ed., McGraw Hill, New York, 1997.

[2] B. C. Nakra, *Vibration Control in Machine and Structures using Viscoelastic Damping*, Journal of Sound and Vibration, Vol 21, No. 3, 449-465, 1998.

[3] T. T. Soong, *Active Structural Control: Theory and Practice*, Wiley, New York, 1990.

[4] A. Premount, *Vibration Control of Active Structures: An Introduction*, 2nd Ed., Kluwer Academic, Dordrecht, 2002.

[5] L. Meirovitch, *Dynamics and Control of Structures*, Wiley, New York, 1990.

[6] G. Gatti, M. J. Brennan, P. Gardonio, *Analytical Models Describing the Coupling Between Piezoactuators and a Beam,* ISVR Technical Memorandum No.923, 2003.

[7] R. M. Jones, *Mechanics of Composite Materials*, Hemisphere Publishing Company, New York, 1975.

[8] C. R. Fuller, S. J. Elliot, P. A. Nelson, *ActiveCcontrol of Vibration*, Academic Press, 1996.

[9] J. S. Burdess, J. N. Fawcett, *Experimental Evaluation of a Piezoelectric Actuator for the Control of Vibration in a Cantilever Beam*, Proc. Instn. Mech. Engrs., 206, 99-106, 1992.